Alma Mater Studiorum · Università di Bologna

School of Engineering and Architecture

Department of Industrial Engineering

B.Sc in Aerospace Engineering

Class L-9

Bachelor Thesis

in

Aerospace Structures

Finite Element Structural and Thermal Analysis of JT9D Turbofan Engine First Stage Turbine Blade

Written by: **Supervisor:**

Davide Boiani   Prof. Ing. Enrico Troiani

Session IIIa
Academic Year 2015/2016

A mio nonno Carlo

To confine our attention to terrestrial matters
would be to limit the human spirit.

Stephen Hawking

Contents

List of Figures

List of Tables

Abstract

The objective of this work was to conduct a preliminary finite element static structural and transient thermal analyses of a first stage turbine blade which was previously assembled on a Pratt & Whitney JT9D-7A turbofan engine. This turbine blade was obtained from a collector of aircraft scrap parts. After an extensive theoretical background on airbreathing jet engines and materials used for such components, the process behind the creation of a 3D model was explained. The laser scanning technique and a piezoeletric digitizer were employed to recreate the blade inside a 3D modelling software. The model was then imported into the finite element analysis software ANSYS; the analyses were performed, and the most interesting results were evaluated. The structural and thermal results were found to be congruous with the literature on similar applications of components with the same material, and appear to be a realistic representation of the blade behaviour inside the first stage turbine environment.

Sommario

L'obiettivo di questo lavoro di tesi e' stato quello di condurre una analisi preliminare sia strutturale-statica che termica-transitoria agli elementi finiti di una paletta di primo stadio di turbina precedentemente appartenente a un motore turbofan JT9D-7A della Pratt & Whitney. Questa paletta e' stata ottenuta da un collezionista di parti di aeromobili. Dopo un esteso background teorico riguardante motori per aeromobili e materiali usati per le palette di turbina, il processo di creazione del modello 3D e' stato esplicato. La tecnica a laser scanning e un tastatore piezoelettrico sono stati impiegati per ricreare la paletta in un software di modellazione 3D. Il modello e' stato poi importato nel software per analisi agli elementi finiti ANSYS; le analisi sono state effettuate e i risultati piu' rilevanti sono stati valutati. I risultati delle analisi strutturale e termica si sono trovati in accordo con la letteratura riguardante simili applicazioni di componenti di quello specifico materiale, e si rivelano essere rappresentazioni realistiche del comportamento della paletta all'interno dell'ambiente di primo stadio di turbina.

In qualita' di relatore autorizzo la redazione della tesi in lingua straniera e mi faccio garante della qualita' linguistica dell'elaborato.

Introduction

The main objective of this work of thesis was to conduct a preliminary finite element static structural and transient thermal analysis of a Pratt & Whitney JT9D turbofan engine first stage turbine blade. The blade was obtained by the author from a collector in Israel. Therefore, the model used for the analyses directly reflects the real geometry of the blade, as a *laser scanning* technique and a *piezoeletric digitizer* were employed to recreate a 3D model of the component.

The goal was achieved by using the finite element analysis software package ANSYS by *ANSYS*, more precisely, the ANSYS Workbench environment.

In the first three chapters, the theory regarding airbreathing jet engines, superalloys and stresses present on a turbine blade was extensively discussed; the properties of the material that composes the blade, which is a Nickel-base superalloy called MAR M-200, were shown. Those values were later implemented into ANSYS, and the a model of the material was recreated for the analyses.

In chapter 4, the process behind the creation of the 3D model which was later used in the analyses was explained in detail. The hardware and software that was needed was presented, together with a brief definition of how these systems operate.

In the last chapter, the step-by-step process behind the analyses was shown. First, the preliminary set-up used for both analyses was explained: how the ANSYS Workbench environment presents itself, how the previously created 3D model was imported into the finite element software and lastly how the final mesh of the model was defined. Then, with regards to the static structural and transient thermal analyses themselves, the setup stage was presented, showing what the loads and the boundary conditions were.

Finally, various results of interest were shown and criticized. These results were presented both with pictures, created directly from ANSYS, and in tabular form, showing the changing values of the results over time; charts of these values were created for better user visualization.

Chapter 1

Airbreathing Jet Engines
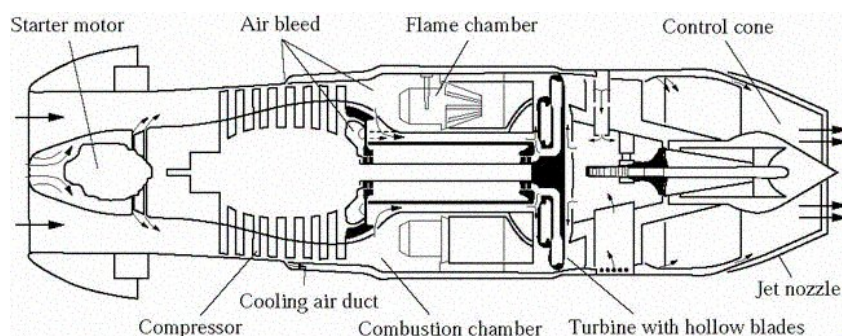
Figure 1.1: Schematic and main components of the Jumo 004B turbojet engine

Since it was first patented by Frank Whittle in Great Britain in 1930, the gas turbine engine has seen an improvement on efficency and performance thanks to the multiple technological innovations introduced over the decades.

The basic principle of airbreathing jet propulsion is simple: it is designed to produce thrust F, and an air mass flow rate $\dot{m}_0$ and fuel $\dot{m}_f$ are responsible for producing this force: through the Newton's action-reaction principle, the fluid that is expelled through the exit nozzle of the engine creates an equal reaction in the opposite direction of this force, thus propelling the aircraft forward. A more detailed mathematical definition of *thrust* will be discussed later in this chapter.

Whittle's engine was based on the Brayton cycle. A double-sided centrifugal compressor compressed the air. Then a combustion took place in a large reverse flow burner (this type of burner was used in order to reduce flame instability) and then a single stage axial turbine powered the compressor shaft.

Meanwhile, in 1936, a german engineer called Has-Joachim Von Ohain invented the first

turbojet engine. During WWII, the first jet engine powered aircraft was introduced, the Messerschmitt Me 262, which carried two Jumo 004B engines.

It presented most of the basic features of more modern turbojet engines: an inlet that drew air inside the engine, an axial compressor, a combustion chamber, an axial turbine and an exit nozzle; even an air cooling system was introduced, bleeding relatively cold air from the compressor in order to reduce the temperature in the first stage of the axial turbine. This engine was able to produce nearly 9 kN of thrust.

As already mentioned, even if the foundation of modern aeronautical propulsion was laid by the Whittle and Von Ohain engines, a lot of improvements have been made by engine manufacturers to improve the most important parameters that define the overall performance of an engine. One of the most relevant to this work is the multispool configuration. This tecnology, developed in the 60s, allows to have multiple concentric shafts spinning at different rotational speeds. Some compressor stages are grouped and coupled with some turbine stages. This means that, in case of a two spool configuration, a low pressure compressor (LPC) could be coupled with a low pressure turbine (LPT), and a high pressure compressor (HPC) with a high pressure turbine (HPT). This allows to have better matching control than in a single spool configuration. Due to inertial forces, the possible rotational velocity has a limit, mostly caused by the different stresses that LP and HP blades are subjected to. So it is desirable to rotate the LP parts at reduced speeds. Three spooled configurations were also developed: in this case, an intermediate-pressure compressor (IPC) is coupled with the respective turbine.

The introduction of this technology led to the invention of a widely used type of engine nowadays, the *turbofan* engine. The core of this type of engine is essentially the same of a turbojet. In this case, an additional LPT has been added: the task of this turbine, which rotates at different speeds from the core gas generator, is to provide power to a fan positioned in the front of the engine. In the late 60s, three spooled configuration of turbofan engines started to appear on the commercial flight market as well. A more detailed explaination of the key parameters that make this type of engine preferrable for commercial flight will be presented in this chapter.

1.1 Engine Thrust Evaluation

It becomes necessary to mathematically evaluate the thrust F in order to better understand the definitions of the most relevant parameters that influence engine efficency and performance.
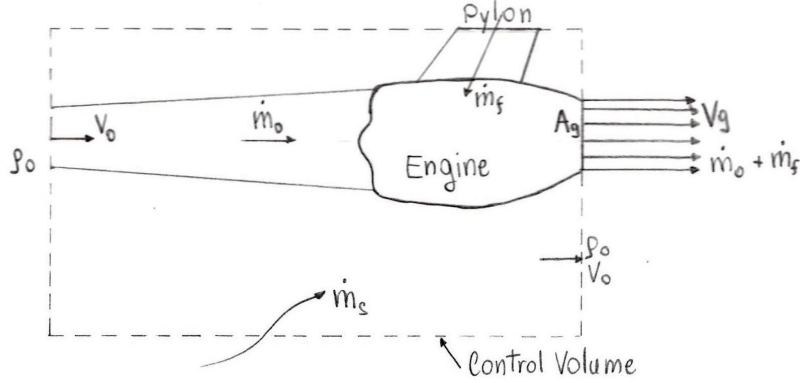
Figure 1.2: Example control volume, flow rates and velocities

The first step is defining an arbitrary control volume around the engine, as shown in Figure 1.2 as an example. Then, by applying the law of conservation of mass to the control volume, is possible to balance the fluid momentum throughout the x-axis. In a steady flow case, the balancing equation is

$$\sum \dot{m}_{in} = \sum \dot{m}_{out} \tag{1.1}$$

Applying this equation to the control volume gives

$$\rho_0 V_0 A + \dot{m}_s + \dot{m}_f = (\dot{m}_0 + \dot{m}_f) + \rho_0 V_0 (A - A_9) \tag{1.2}$$

which simplifies to:

$$\dot{m}_s = \dot{m}_0 - \rho_0 V_0 A_9 \tag{1.3}$$

where ρ_0, V_0 and $\dot{m}_0$ are, respectively, the entry density, velocity and air mass flow rate, A is the box area surface, A_9 the exit nozzle area and $\dot{m}_f$ is the quantity of fuel.
With this information, the mass conservation law can be used, as follows

$$\sum (\dot{m} V_x)_{out} - \sum (\dot{m} V_x)_{in} = \sum (F_x)_{fluid} \tag{1.4}$$

which, after some substitutions, gives the expression of the axial force of the engine, *thrust*

$$\boxed{F = (\dot{m}_0 + \dot{m}_f) V_9 - \dot{m}_0 V_0 + (p_9 - p_0) A_9} \tag{1.5}$$

where p_9 is the pressure at the exit nozzle.

It is now possible to examine the single terms present in this equation. The first term is the *exhaust* momentum through the exit nozzle, and it contributes positively to the engine thrust. The second term is the *inlet* momentum and it represents a drag term, commonly known as *ram drag*, D_{ram}, and has a negative contribution in the equation. The last term is a pressure area term over the exit nozzle area A_9. Its contribution depends on wether an imbalance in static pressure is present in the exit region: this depends on the velocity of the exit flow:

- ▶ if $p_9 < p_0$ the nozzle is overexpanded, only happens in supersonic jets;

- ▶ if $p_9 = p_0$ the nozzle is perfectly expanded, which is the case of all subsonic jets;

- ▶ if $p_9 > p_0$ the nozzle is underexpanded, only happens in sonic or supersonic jets.

After these considerations, Equation 1.5 can be rewritten as follows

$$F = F_g - D_{ram} \tag{1.6}$$

with F_g being the *gross thrust*, grouping the positive contributions of the nozzles. It is now possible to generalize the above equation: in case of multiple streams, for example in a turbofan engine with separate exhausts, it is possible to group all the gross thrusts produced by the nozzles and all the ram drag produced by the inlets to obtain the total thrust of this type of engine:

$$F = \sum (F_g)_{nozzles} - \sum (D_{ram})_{inlets} \tag{1.7}$$

1.1.1 Takeoff Thrust

While the aircraft is taking off, taking the thrust equation, the ram drag can be neglected as the flight speed V_0 is very low. So, during takeoff, the thrust equals the gross thrust:

$$F_{takeoff} \approx F_g = (\dot{m}_0 + \dot{m}_f)V_9 + (p_9 - p_0)A_9 \tag{1.8}$$

For a perfectly expanded nozzle, as $p_9 = p_0$, takeoff thrust is

$$F_{takeoff} \approx \dot{m}_0 V_9 \tag{1.9}$$

as the quantity of fuel $\dot{m}_f$ can be neglected as well. It is notable the fact that during takeoff, the thrust only depends on the captured airflow $\dot{m}_0$.

1.2 Engine Performance Parameters

A series of parameters, like engine thrust or the mass flow rate of air and fuel, are combined to form important performance parameters that can be recognized as the merit figures of an airbreathing propulsion system. The most relevant to this work are defined.

Specific Thrust

The flow rate of air $\dot{m}_0$ is heavily linked to the size of the air intake. Therefore, the amount of thrust produced is proportional to the mass flow rates of fluid throughout the engine. It is interesting to study thrust per mass flow rate as a merit figure, called *specific thrust*, that is

$$\text{Specific Thrust} = \frac{F}{\dot{m}_0} \qquad \text{[N·s/kg]} \tag{1.10}$$

The main target for this parameter is to maximize it, aiming to produce the maximum thrust with the least quantity of air, or equivalently to minimize the engine frontal area. A *nondimensional specific thrust* can also be defined:

$$\text{Nondimensional Specific Thrust} = \frac{F}{\dot{m}_0 a_0} \tag{1.11}$$

where a_0 is the ambient speed of sound taken as the reference velocity.

Thrust-Specific Fuel Consumption

Another merit figure parameter of the engine is, and one of the most important, the ability to produce thrust with the mininum amount of fuel consumption. This ratio is called the *Thrust-Specific Fuel Consumption* (TSFC) and can be mathematically expressed as follows:

$$\boxed{\text{TSFC} = \frac{\dot{m}_f}{F}} \qquad \text{[mg/s/N]} \tag{1.12}$$

As stated, the objective is to minimize this ratio in order to have an efficient propulsion system and more economically profitable, by reducing fuel consumption and therefore fuel costs. Throughout the years, TSFC has seen a significant reduction in comparison to the first jet engines, as seen in Figure 1.3.

Thermal and Propulsive Efficiencies

Two important merit figures are the thermal efficiency and propulsive efficiency. The thermal efficiency is the ability of an engine to convert the fuel's thermal energy
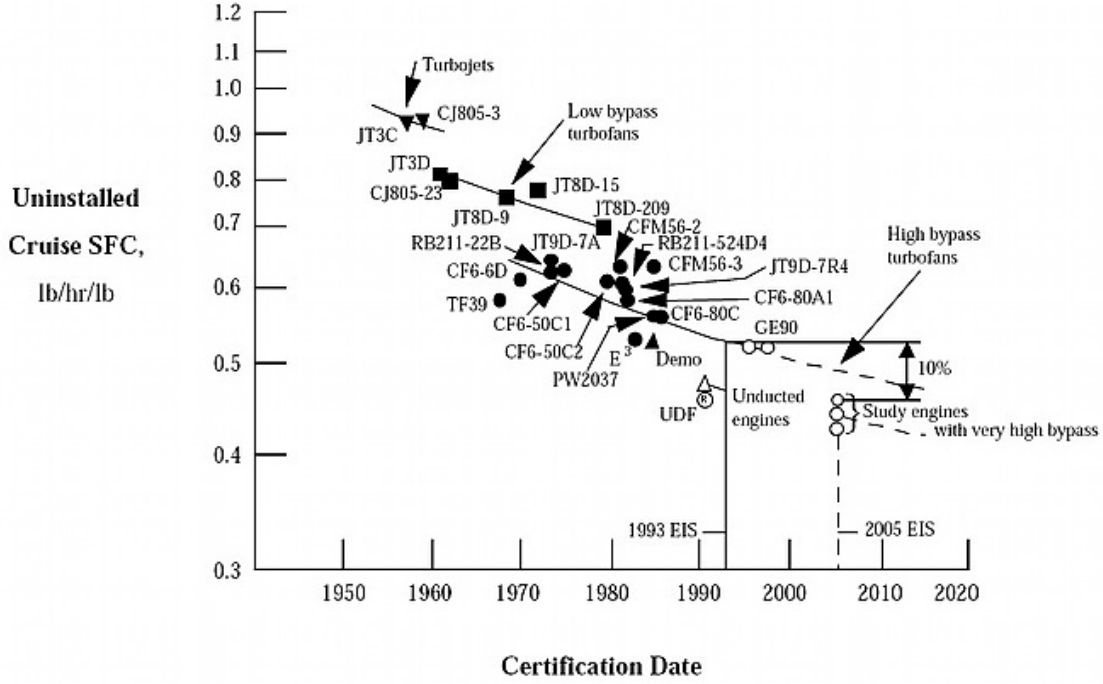
Figure 1.3: TSFC over the years. *Courtesy of NASA*

(released with a chemical reaction) to a kinetic energy gain:

$$\eta_{th} = \frac{\Delta K \dot{E}}{P_{thermal}} = \frac{(\dot{m}_0 + \dot{m}_f)V_9 - \dot{m}_0 V_0^2}{2\dot{m}_f Q_R} \tag{1.13}$$

where $\Delta K \dot{E}$ is the mechanical output of the engine, $P_{thermal}$ is the thermal output power, the subscripts 0 and 9 correspond to the inlet and exit nozzle stations and Q_R is the fuel heating value.

The propulsive efficiency represents the fraction of the mechanical output that is converted into thrust power, that is

$$\eta_p = \frac{F \cdot V_0}{\Delta K \dot{E}} \tag{1.14}$$

which can also be rewritten as velocity dependent only:

$$\eta_p = \frac{2}{1 + V_9/V_0} \tag{1.15}$$

The obvious aim is to maximise both of those parameters, in order to have a better *overall efficiency* η_0:

$$\eta_0 = \eta_{th} \cdot \eta_p = \frac{F \cdot V_0}{\dot{m}_f Q_R} \tag{1.16}$$

1.2.1 Effect of Parameters on Aircraft Range and Endurance

After defining the most imporant parameters that act as merit figures in the design of a propulsive system, it is now possible to evaluate how these parameters directly affect range and endurance of an aircraft.

First, it is imperative to take into account the basic equations of atmosferic flight mechanics, which describe the balanced forces that are able to sustain a level flight cruise:

$$F_{engine} = D_{aircraft} \qquad\qquad L = W \qquad\qquad (1.17)$$

The thrust produced by the engine must overcome the air resistance on the aircraft, and the lift produced by the aerodynamic surfaces (mainly the wings) must balance the weight of the aircraft itself.

It is then possible, after some substitutions, to derive the Breguet range equation, which is applicable under the following preliminary assumptions: the level flight is unaccelerated, the lift to drag ratio is costant, as it is the engine overall efficiency η_0:

$$\text{Range} = \eta_0 \frac{Q_R}{g_0} \frac{L}{D} \ln \frac{W_i}{W_f} \qquad\qquad (1.18)$$

where g_0 is the Earth's gravitational acceleration and W_i and W_f are respectively the initial and final weight of the aircraft (the first one of which is greater than the second, due to the fuel burned during the cruise).

As it can be clearly seen, the range is direcly affected by the overall engine efficiency η_0: it becomes clear why it is important during the design stage of an engine to aim to maximise this value.

The Breguet equation can be rewritten in terms of TSFC, as follows:

$$\text{Range} = \left(M_0 \frac{L}{D} \right) \frac{a_0/g_0}{TSFC} \ln \frac{W_i}{W_f} \qquad\qquad (1.19)$$

where M_0 is the flight Mach number and a_0 is the speed of sound at a given altitude. In this equation, it also becomes clear why another aim of a designer it to reduce as much as possible the TSFC in order to have greater range for an aircraft.

The same thinking can be applied to visualize the effects of η_0 and TSFC on the endurance of an aircraft, defined as:

$$\text{Endurance} = \frac{\text{Range}}{V_0} \qquad\qquad (1.20)$$

being V_0 the current flight speed. With that being said, the same results are achieved: by increasing the overall efficiency and reducing the TSFC, it is possible to achieve greater aircraft endurance as well as range.

1.3 Turbofan Engines

A turbofan engine is characterized by two separate exhausts; the captured airflow is therefore divided into a *core* stream and a *bypass* stream. As already mentioned, the engine has a two-spool configuration, due to different structural loads on the moving parts: the main gas generator has the HPC and HPT connected with the first shaft; a second LPT connects the second shaft with the fan, thus producing the mechanical energy needed for rotation.

For this type of engine, it becomes necessary to define two parameters:

- ► the **bypass ratio** α, the ratio of the flow rate in the fan duct and that of the core, that is

$$\alpha = \frac{\dot{m}_{fan,bypass}}{\dot{m}_{core}} \tag{1.21}$$

- ► the **fan pressure ratio** π_f, the ratio between the total pressure at the fan *exit* and that of the fan *inlet*[1], that is

$$\pi_f = \frac{p_{t13}}{p_{t2}} \tag{1.22}$$

The main asset of this type of propulsion is the fact that by having a larger mass flow rate of air at a smaller velocity increment across the engine, it becomes profitable for having a higher propulsive efficiency (as it can be seen from Equation 1.15) and thrust. Another positive aspect of turbofan engines is a reduced exhaust noise: the low-speed bypass air that sorrounds the core muffles the high-pitched noise of the exit nozzle, resulting in a quieter propulsion unit.

On the down side, to have a high mass flow rate, the frontal area of the engine must be larger than the one in other types of engines. This means that the faster the airplane on which they are mounted is going, the higher the aerodinamic drag will be. However, at subsonic speeds, the positive aspects of turbofan engines outweight the negative effect of drag components on thrust, making it a perfect candidate for the use in commercial aviation.

---

[1]The subscripts refer to the engine schematic shown in Figure 1.4.

1.3.1 The JT9D Turbofan Engine
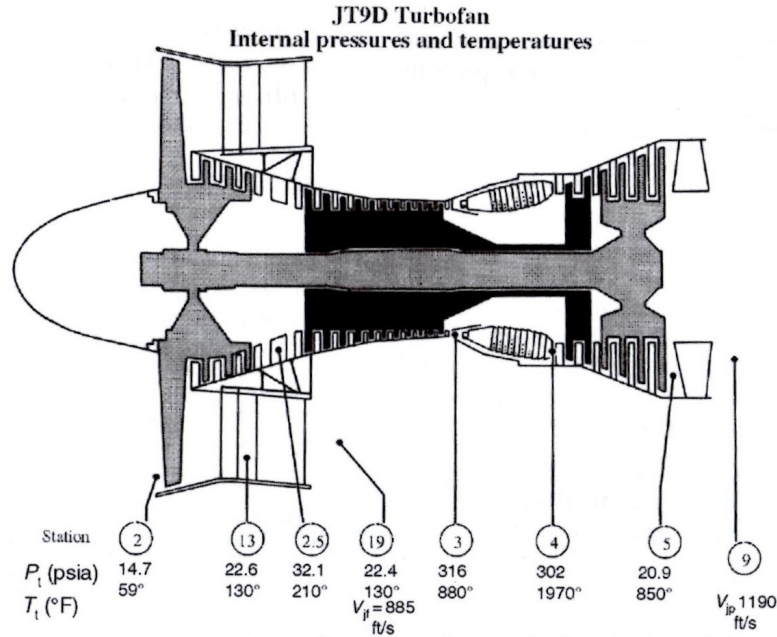
Figure 1.4: Schematic of JT9D engine with different temperature and pressure values

Due to its relevance to this work, an introduction to the main components and characteristics of the Pratt & Whitney JT9D engine series will be carried out.

The P&W JT9D series was first introduced to the industry in the late 1960s and was the first high bypass ratio (HBR) turbofan engine produced by P&W. Its goal was to power a new brand of wide-body airliners that were starting to be used to travel longer distances, mainly the first Boeing 747-100 and, later, 747-200.

Following the first initial testing years, the series grew in order to accomodate different types of aircrafts such as the Boeing 767, the Airbus A310 and the McDonnell Douglas DC-10. After some years of good performance on the market, it was replaced by the PW4000 series of turbofan engines, which were improved versions of the JT9D family.

Specifications

In table 1.1, the most relevant characteristics for the JT9D-7 series can be found. The engine has a two spool configuration and is composed of a 1-stage fan, 3-stage LP compressor and 11-stage HP compressor, an annular combustion chamber, a 2-stage HP turbine and a 4-stage LP turbine. Depending on the model, it is able to produce between 180 kN and 210 kN of thrust at ground level. In the interest of this work, the shaft velocities and turbine entry temperature (TET) will be presented.

11

	Dry Weight	Length	Fan Diameter	Bypass Ratio	TSFC
JT9D-7	3990 kg	3,26 m	2,34 m	5.0:1	61 kg/kN/hr

Table 1.1: Main characteristics of JT9D-7 engine

The low pressure rotor speed, for the JT9D-7 series, is set at 3750 rpm, while the high pressure rotor one is set at 8000 rpm.

The design TET, meaning the temperature of the air flow exiting the burner, varies from engine to engine, and the maximum value of it also depends on the operational state of the engine. In table 1.2 the TET_{max} in different conditions is stated.

	TET_{max}
Maximum continuous	880 °C
Maximum acceleration	915 °C
Takeoff (5 min)	915 °C
Starting	650 °C

Table 1.2: Turbine Entry Maximum Temperatures

1.3.2 Brief Analysis of Turbofan Engine Thermodynamic Cycle
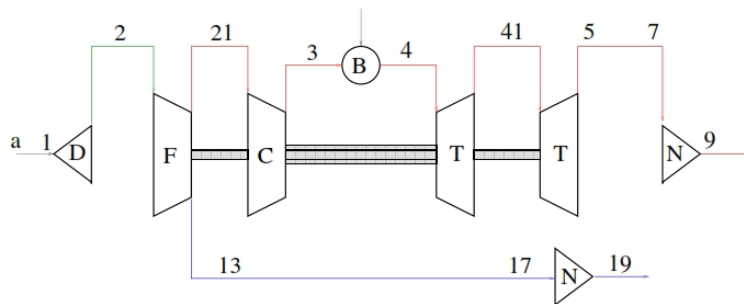
Figure 1.5: Schematic of turbofan engine with separate exhausts

In this section, a brief overview of the Brayton cycle of a typical turbofan engine will be carried out.

A simplified schematic of the turbomachinery inside a turbofan is depicted in Figure 1.5: the two-spool configuration is visible, along with the main components of the engine (D is the intake, F is the fan in which the optional LP compressor is inherently included, C the compressor, B the combustion chambers, T the turbines and N is the nozzle, split to

represent the two separate flows).

Then, in figure 1.6, a typical separate flow turbofan engine temperature-entropy Brayton cycle is depicted[2]. First, the air enters the engine through the inlet, which is the curve
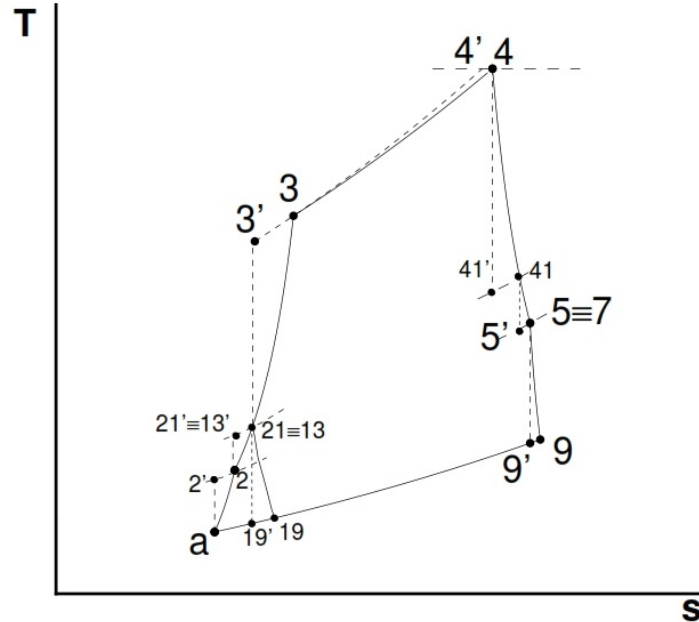
Figure 1.6: Brayton cycle of a turbofan engine

from **a** to **2** represented on the diagram. In this phase the air is slightly compressed and the temperature starts to rise. Then the air flow passes through the fan and enters the LP compressor (from **2** to **21≡13**) in which the air is further compressed. Note that the fan behaves exactly like a LP compressor (in fact, in the case of the JT9D-7 engine, the fan pressure ratio is 1.64:1). The air flow later enters the HP compressor, in which the air is further compressed and heated (from **21≡13** to **3**) and goes in the combustion chamber (which presents a nearly isobaric process) to maximise the temperature value at point **4**. The air flow then enters the HP turbine at high temperatures (from **4** to **41**) and the LP turbine (from **41** to **5≡7**) while expanding the air and cooling it by transfering pressure energy into mechanical energy used to power the shafts. The final step is the nozzle, in which the two flows mix together again, dropping the pressure at the moment of exit to the value of the external air (from **5≡7** to **9**).

---

[2]It is to be noted that in the diagram the ' over a number represents the isoentropic thermodynamic process associated with that state

1.4 Turbine Blades

Due to their positioning in the propulsion unit, the turbine blades are among the most stressed components in the entire system.

The turbine is the gas generator component appointed to produce the shaft power needed to the compressor or, for example in a turbofan, the fan. The air flow from the combustion chamber, having high temperatures and pressures, produces an enormous amount of thermal and mechanical stresses on the blade disks and the turbine blades themselves.

After entering the HP turbine, the air flow first passes through the stator turbine nozzle, which is of course exposed to the highest temperatures of the whole engine (in the order of $\sim$1500-2000 °K). Then the air flow goes through the first stage of the turbine (is called stage the combination of an adiacent rotor disk to a stator disk), encountering first a row of rotor blades which, in addition to extreme thermal stresses, are subjected to a centrifugal acceleration caused by the elevated rotational velocity of the disk.

As a matter of fact, nowadays the first stage of the turbines operate at 500-700 °K higher than blade service temperature. So, it becomes a necessity for the blade to be cooled. The coolant is bled from stages of the compressor, and represents $\sim$10-15% of the total air flow. A near 3% of turbine efficiency reduction can be attributed to losses due to cooling per every 1% of cooling flow. Therefore, the primary challenges in the turbine are the optimization of cooling effectiveness and the study of the different techniques; the blade life expectations and the use of the most suitable materials to sustain a very high temperature environment.

In figure 1.7[3], a schematic drawing of the velocity profiles across a stage is shown. As already mentioned, a turbine stage begins with a stator blade row and is followed by the rotor blade row. In the stator, the air flow is accelerated, converting fluid thermal energy into fluid kinetic energy. The stator blade row gives a swirl to the flow (meaning the air flow is given a rotational velocity component); then the flow passes through the rotor blade row, exchanging energy with it, removing the afore mentioned swirl.

It is also possible to examine the *zero exit swirl* configuration, as shown in Figure 1.8[4], along with the consequent variations across the stations (1-2-3) of temperature, pressure, density, total temperature, total pressure and velocity components: in this case it does not contribute in the production of thrust, but it increases the total pressure drop in the stator, making it a more desirable configuration.

---

[3] *Courtesy of Farokhi (2014).*

[4] See footnote 3.

Figure 1.7: Blade rows and velocity triangles

Figure 1.8: Blade rows for a *zero exit swirl* design

1.4.1 Turbine Cooling Techniques

In this section, a classification of the main cooling techniques will be carried out.

As already mentioned, the TET of modern airbreathing engines is far higher than the maximum operative limits of metals, even very high temperature-resistant nickel-based superalloys used in aeronautics. Therefore, the need to cool the first two, or even three, stages of the turbine becomes highly relevant. The cooling fluid comes from directly from the compressor.
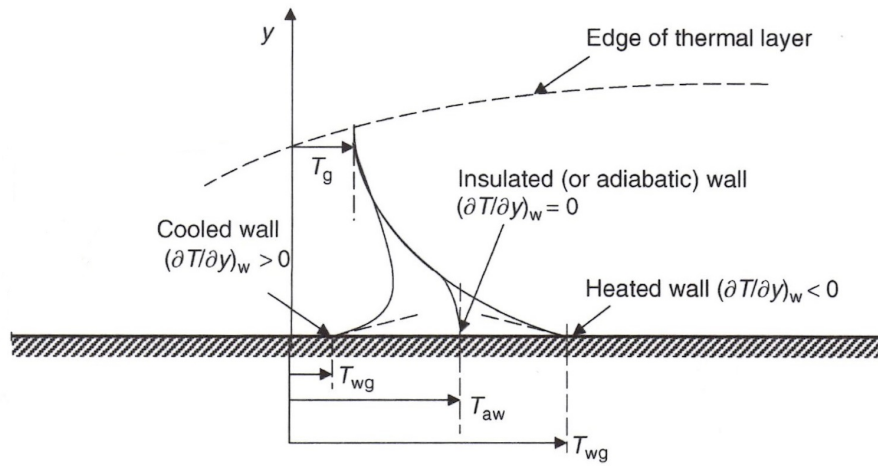
Figure 1.9: Temperature distribution on the wall inside the thermal layer

The Fourier law of heat conduction governs the temperature distrubution in the thermal layer:

$$q_y = \frac{\dot{Q}}{A} = -k\frac{\delta T}{\delta y} \qquad [\text{W/m}\cdot°\text{K}] \qquad (1.23)$$

where q_y in the heat flux, $\dot{Q}$ is the heat transfer and A the area, k the thermal conductivity and $\frac{\delta T}{\delta y}$ is the temperature gradient in the y direction. The negative sign forces heat to flow from hot to cold. Three cases are possible:

$$\left.\frac{\delta T}{\delta y}\right|_{y=0} = 0 \qquad \text{for an insulated wall}$$

$$\left.\frac{\delta T}{\delta y}\right|_{y=0} < 0 \qquad \text{for a heated wall}$$

$$\left.\frac{\delta T}{\delta y}\right|_{y=0} > 0 \qquad \text{for a cooled wall}$$

These represent the different boundary conditions of static temperature distribution at the wall (Figure 1.9).

Some of the techniques used to cool the blade are:

▶ Radiation cooling;

▶ Convective cooling;

▶ Impingement cooling;

▶ Coating the surface with a protective low-thermal conductive layer of ceramic coating;

▶ Film cooling;

▶ Combination of various methods above.

The most relevant will be briefly explained in the next pages, along with their effects on overall turbine efficiency.

Convective Cooling

By using the convective cooling technique, the interior passages of the blade are divided into five parts: the first is at the leading edge of the blade, known as the nose section; it is then followed by three central sections and one traling edge section. In between these sections, the relatively cooler bleed air of the compressor passes through the passages, exchanging heat with the internal blade wall, thus cooling the blade.

The heat exchange is governed by the Newton's law of cooling:

$$q = h\Delta T \tag{1.24}$$

where h is the coefficient of heat transfer and ΔT is the temperature difference.

Also, it is preferrable to position inside the passages an array of "pins" (or ribs), normal to the fluid flow direction, in order to "disturb" the air flow as much as possible, making the flow more turbulent.

Impingement Cooling

Convective cooling is often coupled with impingement cooling. It is to be noted that the leading edge (or stagnation point) of the blade is the most thermically influenced part of

the component, having the hight heat flux area in the blade. Also, heat transfer rapidly rises due to boundary layer transition from laminar to turbulent. This is done in order to reduce the local skin friction coefficent, which is directly proportional to the Reynolds number.

So, in order to cool this critical part of the blade, the internal passage of leading edge presents a series of holes that collide with the internal face of the blade, thus cooling the leading edge.

Film Cooling

Another effective cooling technique is film cooling. In the most critical areas of the blade (for example the leading edge) a row of holes is present in order to create a film of coolant around the external wall of the blade, thus protecting the blade from the high temperatures. The coolant flow is ejected through the holes, which have a precise angle with respect to the external flow, and is bent around the blade, creating the protective film. It is obvious that by expelling fluid outside of the blade has a more negative effect on the overall aerodynamics of the turbine compared to the above discussed internal cooling. In order to cover all of the surfaces that need cooling, rows of holes across the blade are positioned, as the film cooling effect is notable only in the vicinity of the single hole.

Hole diameter varies from 0.5 to 1 mm; even though a smaller hole diameter is technologically possible, it is not recommended, as such small holes are eager to get clogged in the extreme turbine environment due to residual particles and by-products from the combustion.

1.4.2   Effects of Cooling on Turbine Efficiency

After all these considerations, it is possible to make a small but very important list, in which the most relevant negative effects that cooling of turbine blades and disks can have on the overall efficiency of the turbomachinery.

▶ The coolant that is bled from the compressor does not produce turbine power; so due to loss of working fluid, per 1% cooling fraction, a near 1% loss in power production is expected;

▶ The injection of the coolant inside the flow causes losses and increases the profile drag, due to flow disruption on the surface of the blade;

18

▶ The coolant suffers a pressure decrease inside the passages in the blades due to surface roughness, increased friction, pins, etc. It causes the stage total pressure ratio to decrease.

It is tipically estimated a loss of ~2.7-3.2 % of turbine efficiency drop per 1% of cooling flow.

Chapter 2

Turbine Blade Stresses and Progress in Materials

One of the most important charateristics of the aeronautical engines that made possible incredible progress in overall performance is the constant advancement in high-temperature materials research, and the related studies on fenomena occurring in a high structural and thermal stress environment such as the first stages of the HP turbine. In the last decades, one of the industry's main focuses has been on the structural design of an engine. The aim is to reduce the components weight, complexity and cost, while meeting the structural, aerodynamic and thermodynamic requirements. The engine total life is heavily impacted by changes like these. Depending on the mission the engine will be tasked to do, designers can make better decisions regarding these changes, by being able to simulate the operative use the engine will have, thus demonstrating the required durability.

Overall performance continuous increase of the aircraft power plants over the years has been strictly correlated with the increase of the TET, achieving greater combustior exit gas temperature, thanks to advancement in materials used in critical parts of the engine and better cooling techniques of the first stages of the turbine. In the very first decades of use of airbreathing engines, the turbine was not cooled by the bleed air from the compressor, resulting in a very strict limit on TET, also caused by the properties of the materials used. Turbine cooling was first introduced in a series of Rolls Royce engines. This event made the use of a TET a lot higher than the material melting point possible, being able to achieve higher trust and performances. Another turning point in engine development history was the introduction of the first by-pass turbofan engine, also by

Rolls Royce, in the first years of the 1960s; this technology was improved in the later years, and the high by-pass ratio turbofan JT9D engine was introduced, a propulsion unit that worked with a high pressure ratio and high TET that was able to produce higher thrust, a decrease in TSFC and less exhaust noise, as already mentioned in Chapter 1.

As said above, turbine blade materials play a very important role in the possibility of improvement in maximum TET. In figure 2.1, the advancements over the years of turbine blade materials, alongside with the techniques used to cast these critical parts of the engine, were compared with their impact on the maximum take-off TET that was made available to the engines.
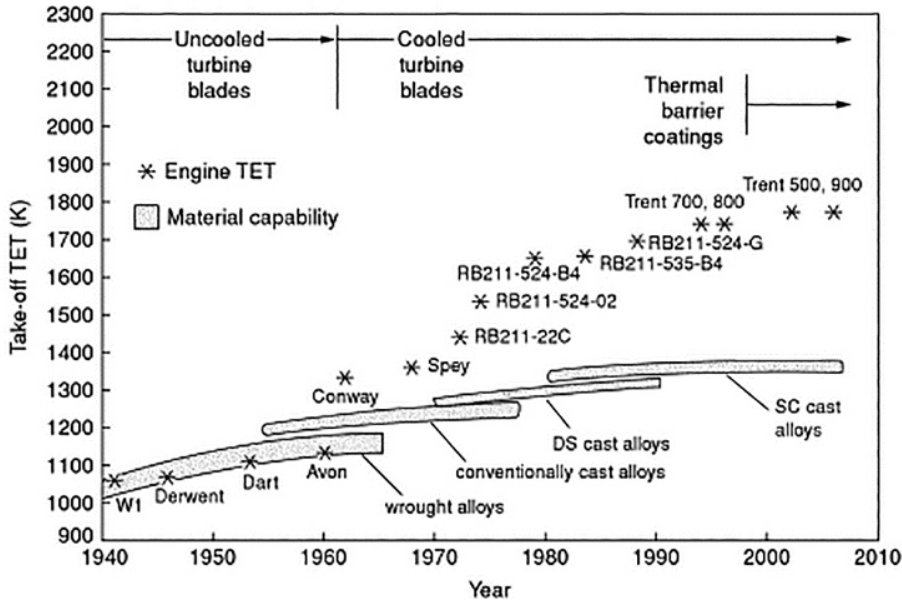
Figure 2.1: Increase of TET over the years due to material technology advancements

The grey strips represent the materials melting point, while the stars in the graph represent the TET of that particular engine. It is notable that, thanks to advancement in cooling techniques, the engines are able to operate with higher and higher temperature gap in comparison to the material operative limits.

The casting techniques of turbine blades have greatly changed over the decades. The first blade were "conventionally" cast, having good mechanical properties in all directions and an equi-axed crystal structure. Then, advancements made possible directionally solidified blades, or columnar grain blades: this methodology improved the

mechanical properties along the longitudinal axis, as the blade presented a columnar crystal structure. The most studied and researched to this day are single crystal turbine blades, which present excellent mechanical properties along the longitudinal axis and an improved heat resistance.
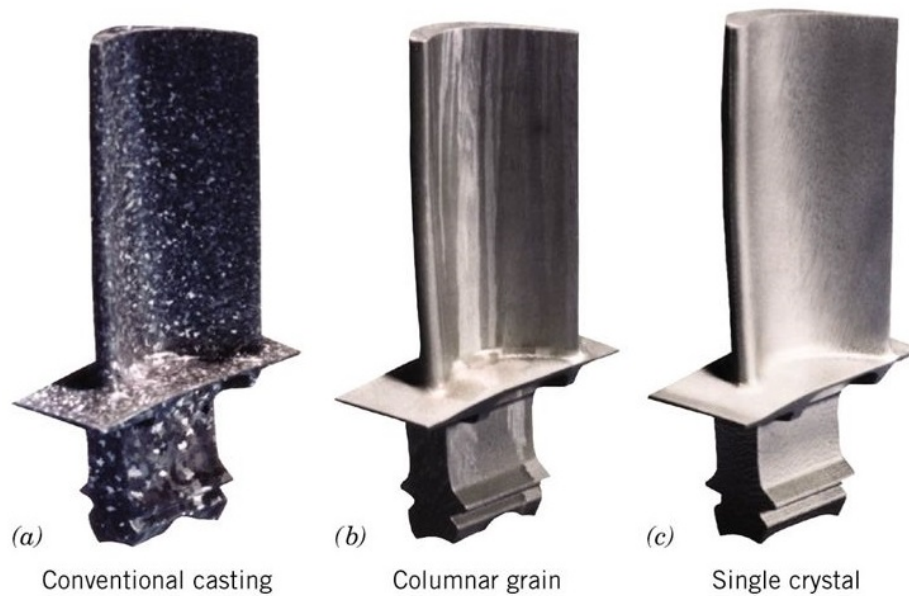
Figure 2.2: Comparison of the various casting typologies

Alongside these technologies, coating technology, like aluminide or overlay coating, plays a key role in reducing the surface operating temperature, thus significantly increasing the component life (at constant coolant flow) or increasing the TET (at constant blade temperature). These coatings are low thermal conductivity materials, that reduce the heat transfer to the turbine blades. With a rough estimation, they reduce the turbine blade surface temperature by 150 °K, and the use of these barriers could potentially save big airliners hundreds of millions of dollars in fuel cost.

Overall, the critical properties that a turbine blade is required to possess are: creep strength, thermal fatigue strength, oxidation and hot corrosion resistance. Its design must also address low and high cycle fatigue, which are among the most common failure to which the blade could be subjected during its operational life.

2.1 Stresses on Turbine Blades

As it has already been mentioned before, turbine blade are subjected to various types of extreme stresses. The main source of stress for these components is the centrifugal force given by the high rotating velocity to which the blades are spun. The force experienced by the blades while the engine is in its maximum operational state can well exceed the enormous amount of 30,000 g of intensity.

The blades also experience other types of stresses, which can damage (or destroy) the component and reduce its operative life, and must be accounted for in the design process. Some of the most relevant are:

▶ **Pressure differences** across the blade, causing airfoil bending moments which can permanently damage the component;

▶ All rotating turbomachinery can experience unsteady **aerodinamic forces**, such as high cycle fatigue (HCF), as a result of non uniform flows; this phenomenom has become the leading cause of failure, especially in military aircrafts;

▶ **Thermal differential stresses** and **low cycle fatigue** (LCF) must also be taken into serious consideration. As mentioned, thermal stresses caused by important temperature gradients, as happens in cooled turbine blades, can create unexpected local stresses on the part, because of uneven expansion and contraction of the material. These severe gradients especially happen during the transaction of the engine from a power setting to another. These stresses are the main cause of thermal fatigue and LCF, which can quickly consume the hot part's life;

▶ **Cracks**, which growth and propagation can seriously reduce the component's life, concentrating high amounts of stress in small parts of the blade;

▶ **Foreign object damage** (FOD), meaning objects that enter the engine from the outside and damage or destroy parts of the propulsion unit, are an unpredictable source of concern. The objects, even small ones, can create cracks which, coupled with the high temperature and stresses that the engine is normally subjected to, can be propagated with the help of HCF, significatly reducing component life;

▶ During severe maneuvers or hard landings, **inertial forces** caused by these movements can be generated within the engine, damaging, for example, the tips of

the rotating turbomachinery or their rotating seals, especially when the clearences are very small, like in the turbine;

▶ Low **torsional stresses** are inevitable and occure as power is transferred by shaft torque to the compressor;

▶ **Erosion**, **corrosion** and **creep** must also be addressed, usually with regards to material composition used for rotating parts.

Different parts of the blade can be subjected to different types of failure: for example, the blade tip can suffer oxidation, corrosion and LCF, while the root of the blade can suffer rupture or HCF.

2.1.1   Centrifugal and Thermal Stress Evaluation

As already said, the most dominant stress in a turbine rotor blade row is the centrifugal stress σ_c. A representation of the stress on a blade is represented in figure 2.3[1].
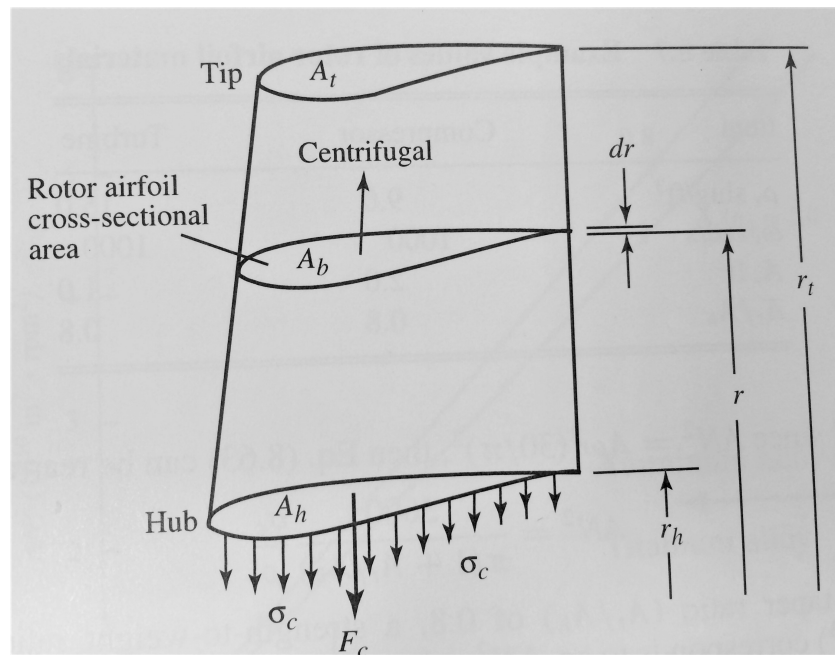
Figure 2.3: Centrifugal stress on blade and nomenclature

The stress can be expressed as follows:

$$\sigma_c = \frac{F_c}{A_h} \tag{2.1}$$

---

[1] *Courtesy of Mattingly, Heiser and Pratt (2002).*

with F_c defined as

$$F_c = \int_{r_h}^{r_t} \rho_{blade} \cdot A_b(r)\omega^2 r dr \tag{2.2}$$

So σ_c can be rewritten as

$$\sigma_c = \frac{1}{A_h} \int_{r_h}^{r_t} \rho_{blade} \cdot A_b(r)\omega^2 r dr \tag{2.3}$$

$$\frac{\sigma_c}{\rho_{blade}} = \frac{\omega^2}{A_h} \int_{r_h}^{r_t} \cdot A_b(r) r dr \tag{2.4}$$

$$\frac{\sigma_c}{\rho_{blade}} = \omega^2 \int_{r_h}^{r_t} \frac{A_b}{A_h} r dr \tag{2.5}$$

A_b/A_h is known as the *taper* ratio and is normally approximated to be a linear function

of the span, as follows

$$\frac{A_b}{A_h} = 1 - \frac{r - r_h}{r_t - r_h}\left(1 - \frac{A_t}{A_h}\right) \tag{2.6}$$

A further approximation is usually done in these calculations, placing the variable r by the pitchline radius r_m. The result is

$$\boxed{\frac{\sigma_c}{\rho_{blade}} = \frac{\omega^2 A}{4\pi}\left(1 + \frac{A_t}{A_h}\right)} \tag{2.7}$$

with $A = 2\pi r_m(r_t - r_h)$ being the flow area, ω the angular velocity and σ_c/ρ_{blade} is a material property known as the *tensile specific strengh*.

One of the most important material characteristic that interest engine designers is the *creep rupture strength*. It is the maximum tensile stress that the material is capable of resisting without failing over a time, while at a given operating temperature. Mattingly, Heiser and Pratt (2002) have plotted the allowable stress versus temperature and allowable strength to weight ratio for various types of materials most used in aeronautical engines (Figure 2.4 and Figure 2.5)[2].

---

[2] 1 ksi $\approx$ 6.865 MPa
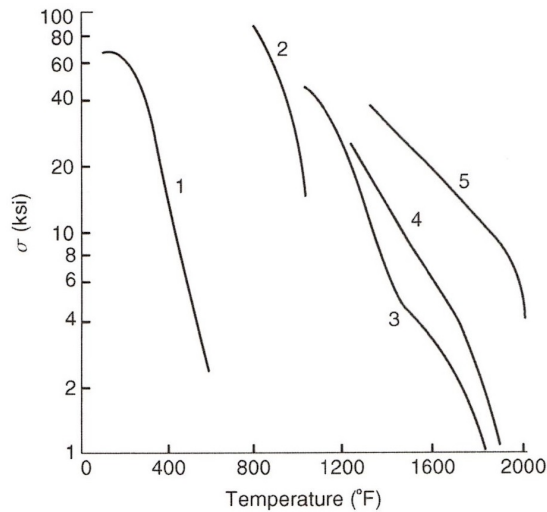
Figure 2.4: Allowable strength over temperature for engine materials
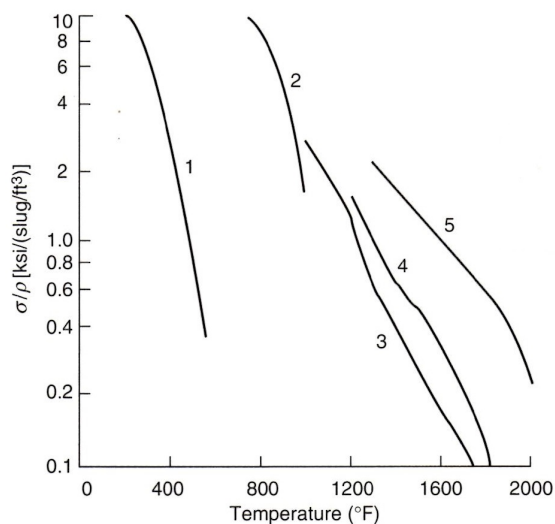
Figure 2.5: Allowable strength to weight ratio over temperature for engine materials

Number	Material	Most used in
1	Aluminum alloy	Structural components, etc.
2	Titanium alloy	Casing, HP compressor disks and blades, etc.
3	Wrought nickel alloy	Turbine blades and disks
4	High-strength nickel alloy	Turbine blades and disks
5	Single crystal superalloys	Turbine blades and disks

Table 2.1: Materials considered in the above graphs

Meanwhile, thermal stresses are evaluated based on thermal strains in a material with a temperature gradient:

$$\epsilon_t = \alpha \Delta T \qquad (2.8)$$

where ϵ_t is the thermal strain and α is the linear coefficient of thermal expansion. Therefore, the thermal stress must obey the stress-strain relationship, so:

$$\sigma_t = E\epsilon_t = \alpha E \Delta T \qquad (2.9)$$

where E is the modulus of elasticity of the material.

The total stress of the material σ_{total} is the sum of all of the stresses to which the material is subjected, like centrifugal, thermal, vibratory, gas loads stresses. Together with the material operating temperature, an estimate of material useful life can be done and put into stress-temperature-life curves for a given type of material.

Chapter 3

An Overview of Superalloys

Since the 1920s and 1930s, the need had arisen for the various high-temperature applications of metals to have certain material properties. Back in those years, stainless steels were very common for such environments, and they became a starting point for the advancements in metallurgy that followed. In fact, steels were quickly found to have limited strength capabilities and low resistance to the phenomena that occured in such hostile environments. With the introduction of the airbreathing jet engine in WWII, the drive to find a replacement for these alloys spread. The industry was introduced to the so called superalloys, materials with a base of iron (which are the least expensive), nickel or cobalt, mixed opportunely with other materials. These superalloys were found to be particularly adequate for their use at high temperatures (generally above 550 °C). At very high temperature, like in a turbine of an aeronautical engine, the nickel base superalloys are the preferred choice, adequately coupled with cooling techniques; it is to be noted that normally the operative range of the superalloys does not exceed the melting temperature of the material, but nickel base superalloys can be used at a higher temperature than the one at their melting range. Some type of superalloys can also find applications in extremely cold environments, like in the space sector. Therefore, the versatility of these alloys is clearly very high.

The strength capabilities of a superalloy are not only closely affected by the chemical composition of the alloy, but also by the melting procedures and the heat treatment that follows the creation of the material.

Alongside their mechanical properties, superalloys show great oxidation resistance in many cases, but lack in corrosion resistance. This is the reason why at very high temperature applications like in a jet engine, the components have the necessity to be coated. The

coating allows the component to correctly operate at very high temperatures for prolonged periods of time without encountering corrosion problems.

In a typical aeronautical engine, superalloys can be found in various components: disks, cases, vanes, blades, combustor afterburners, etc... Their importance is underlined by the fact that, in the 1950s, just 10% of the weight of the propulsion unit was made by these materials, whereas by 1985 the very same percentage increased to a stunning 50%[1].

Superalloy Forms

There are mainly two forms of superalloys: **wrought** and **cast**.

The first generally starts with a cast billet that has been deformed and reheated in order to reach its current state. These are usually more omogeneous than cast alloys, and often considered more ductile. This form of alloys are usually employed in the intermediate temperature disks of a jet engine.

Meanwhile, cast alloys can be found in the hottest parts of the engine, like in blades and vanes. They can be polycrystalline or directionally solidified. The key difference between the two resides in the grain size and positioning. While PC castings contain grains that vary in size from one component to another, DS casting have a more organized grain distribution along the longitudinal axis (which is, for example, in the direction of the centrifugal force in a turbine blade), in which the grains are all parallel to each other. These are best known as Columnar Grain Directionally Solidified (CGDS) components. Single Crystal Directionally Solidified (SCDS) parts also fall into this category, with the main difference of having only a single grain.

At high temperatures, cast alloys favor strength more than wrought alloys, being able to possess greater creep rupture strength. Wrought alloys favor higher yield and LCF strengths at low/intermediate temperatures, explaining their use in disks.

3.1 Crystal Structure and Phases of Superalloys

With regards to crystalline structure, metals have relatively simple ones. The atoms positioning are ordered in three main alignments: face-centered cubic (**fcc**), body centered cubic (**bcc**) and hexagonal close-packed (**hcp**), as seen in Figure 3.1[2].. The ordering is very relevant to superalloy strengthening.

---

[1]*Donachie and Donachie (2002)*

[2]*Courtesy of Donachie and Donachie (2002)*
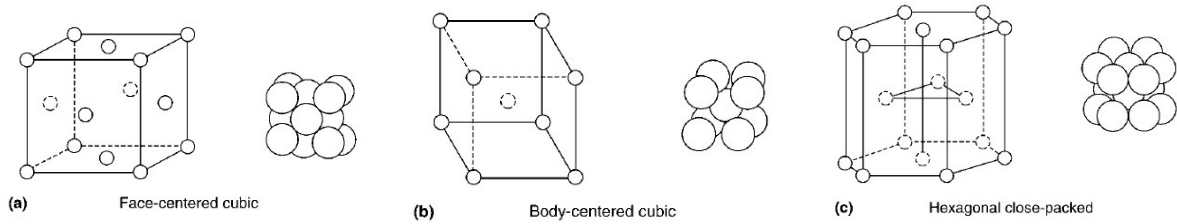
Figure 3.1: Types of superalloy crystalline structures

All superalloys consist of the austenitic[3] fcc matrix phase **gamma** (γ) and a variety of secondary phases. These phases are those which give the alloys their characteristics, thanks to their manipulation and control, together with the grain size and the morphology of the material. Furthermore, the strength of the superalloys mainly derives from strenghtening precipitate phases such as γ' and γ''.

The γ' is the main strengthening phase for most nickel and nickel-iron base superalloys; its size varies with temperature and is normally found in spherical or cuboidal forms. Its morphology can be changed with the introduction of molybdenum and variations in the aluminum/titanium ratio. In this phase, prolongued exposure to very high temperatures (>700 °C) can cause the formation of unwanted η (which may form between the grains in a cellular form) and δ phases.

Also, carbides, which are found in every superalloy, help to stabilize grain boundaries against elevated shear stresses. Elements are opportunely added in order to promote the formation of these phases, together with other elements that better the mechanical properties of the alloy.

3.1.1 Main Properties of Superalloys

For what concerns the physical properties of superalloys, meaning the specific heat, the thermal conductivity, thermal expansion and electrical conductivity, they tend to be lower than those of other metals. These properties are directly influenced by the chemical composition of the alloy.

The superalloys are relatively ductile, even though cobalt base superalloys are less ductile that nickel and iron nickel superalloys. Typical values for the moduli of elasticity is around $30 \cdot 10^6$ psi ($\sim$ 200 GPa) but for PC alloys can vary between 25-35 $\cdot 10^6$ psi (172-241 GPa)

---

[3]Austenitization means that the iron-based metal is heated to a temperature at which it changes crystal structure to austenite. An incomplete austenitization can leave carbides inside the matrix.

depending on the superalloy. For DS precesses it varies between 18-45·10^6 psi (124-310 GPa) depending on the crystal orientation.

As already mentioned, superalloys possess exceptional mechanical strength, resistance to oxidation and corrosion and to thermal creep deformation. These properties are developed by a particular alloying method called *solid solution strengthening*, a process that by adding atoms of other elements to the base metal of the alloy forms a solid solution. The non uniformity that is created disadvantages plastic deformation of the material. Another technique that is deployed, especially in superalloys that are used in very high temperature environments, is *precipitation strengthening*, a heat treatment that forms secondary phase precipitates, like the aforementioned γ' phase and carbides, which provide exceptional mechanical properties for high temperature applications.

Oxidation and hot corrosion resistance are among the most important and not negligible properties of the superalloys. At the high temperatures at which these alloys will be employed, the effects of corrosion become non neglectable. Oxidation can cause the rapid degradation of the alloy by forming cracks that, over time, produce erosion of the component, changing the nominal chemical composition of the alloy, due to the consuption of elements inside the alloy or by increasing the fragility of the material due to introduction of oxide phases, that can promote formation of cracks and fatigue failure.

Nickel Base Superalloys

The main phase that composes these types of superalloys, which have a nickel base matrix, is, of course, the γ phase, a solid solution fcc austenitic phase. The alloying elements that can be found in most of nickel base superalloys are C, Fe, Al, Ti, Mo, W, V and Ta.

The majority of nickel base superalloys are strengthened by the precipitate γ', while for other is γ'' or both. Carbides phases are formed as well. These phases are usually harmful to the material (as in cobalt base superlloys), but in nickel based superalloys they help to stabilize the material structure against thermal deformations caused by high temperatures, but restraining the grain boundary movement. Other phases that can be present are topologically close packed phases, like the σ, μ or χ phases. They form due to prologued periods of time at very high temperatures. These phases tend to consume the γ phase of its strengthening components and increase the fragility of the material. Examples of these alloys are Hastelloy X or IN-625.

In Figure 3.2[4], a typical fcc crystal structure of a γ' phase is represented. The darker

---

[4]*Courtesy of Donachie and Donachie (2002)*
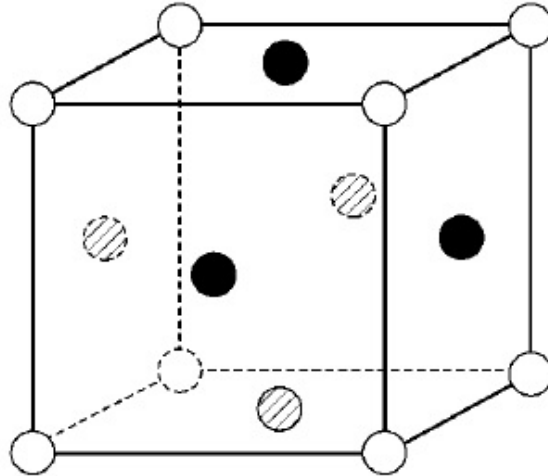
Figure 3.2: Crystal structure of a $\gamma^{'}$ phase

circles represent the nickel atoms (as well as the circles with diagonal lines on the inside), while the white circles represent the aluminum or titanium atoms. This phase, between 600-850 °C, transforms into the η phase, while for temperatures below 600°C the $\gamma^{''}$ phase could be used for strengthening.

These superalloys can be found both in cast or wrought form, even if for the wrought form, a special processing like powder metallurgy is often used. An important role is played by grain control which, with the introduction of directional solidification, has been demonstrated to enhance properties of the alloy.

3.2 Coating Technologies

As already mentioned numerous times, the TET of aeronautical engines exceeds the melting range of temperatures for superalloys employed in the turbine sections of the engine. Therefore, specific techniques must be deployed in order to allow the full capability for the component to operate under the constant threat of oxidation and corrosion. The most common is the use of superalloy coating. There are main three types of coating technology that have been used throughout the years:

▶ Diffusion coatings;

▶ Overlay coatings;

▶ Thermal barrier coatings (TBCs).

These coatings all have in common some characteristics, like having a good reistance in a high thermal stress environment; they must be thin and uniform; they must be relatively ductile in order to withstand the thermal deformations that occur in the substrate to which they are applied and must not influence the mechanical properties of said substrate.

Diffusion coatings, or aluminide coatings, develop an aluminide outer layer which has good oxidation resistance, by reacting with the base metal (being nickel or cobalt). This resistance is created by the formation of oxide scales. These coatings are generally very thin (50-75 μm). They are deposited at intermediate temperatures on the superalloy, and then undergo a very high temperature process before being put into service.

Overlay coatings, referred to as MCrAlY coatings, are more costly to produce due to the processes employed to make them. The "M" in the formula can be Fe, Ni, Co or NiCo. These coatings undergo a very high temperature treatment as well, in order to omogenize the coating on the component. They are nearly twice as thick as diffusion coatings.

Meanwhile, TBCs are essentially composed of two parts: a bond coat and a thermally insulating coat on top, normally ceramic. The bond coat is usually MCrAlY (where "M" can be Ni or NiCo), protecting the substrate from necessary hot corrosion and oxidation. They are able to reduce thermal loads and surface temperature of the component by a factor of hundreds of degrees centigrade. In Figure 3.3, a cross section of a typical TBC/bond coat system is shown.
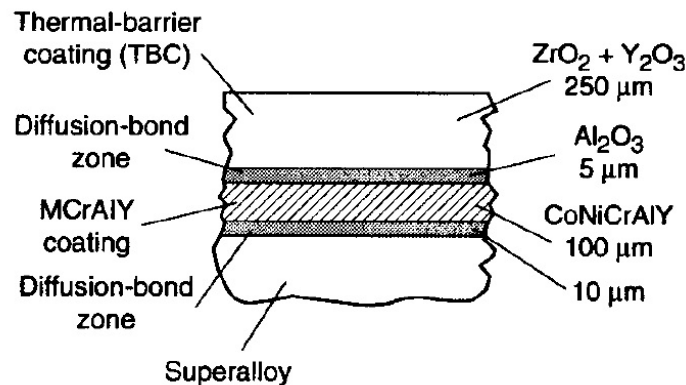
Figure 3.3: Representation of the layers of a TBC and their thickness

3.3   MAR M200 Nickel Base Superalloy

Due to its relevance to this work, the MAR M200 superalloy will be presented.
MAR M200 is a cast polycrystalline nickel base superalloy largely used in the 1970-80s
as a standard material in first and second stage turbine blades. A notable example is its
application on the P&W JT9D series of turbofan engines, described in Section 1.3.1. Its
usual chemical composition is shown in Table 3.1.

	Chemical composition (%)								
	C	Ni	Cr	Co	Fe	Al	B	Ti	W	Zr
MAR M200	0.15	59	9	10	1	5	0.015	2	12.5	0.05

Table 3.1: Chemical composition of MAR M-200 superalloy in weight percentage

The blades that were made with MAR M200 were usually directionally solidified;
variations of this superalloy were later introduced, like DS MAR M200 + Hf (hafnium),
which was found to have improvements in transverse grain boundary strength and
ductility. Work on a single crystal variant of this superalloy was done, but discontinued
as did not offer enough improvements on material properties and were more expensive to
produce[5].
To enhance solid solution strengthening and the formation of carbides, a 12.5% of
tungsten was added; the presence of cobalt (10%) increases the solubility temperature;
chromium (9%) increases the oxidation resistance and improves the high temperature
capabilities of the superalloy[6].

Dandekar et al. (1981), using a sonic resonance technique, were able to determine
the variation of Young's modulus and the shear modulus of the superalloy with
temperature, as shown in Figure 3.4. Alongside the moduli, three values of the Poisson's
ratio were presented for three different temperatures, as shown in Table 3.2.

	Poisson's Ratio		
	300 °K	970 °K	1125 °K
MAR M200	0.354	0.368	0.375

Table 3.2: Poisson's ratio increase with temperature

---

[5]Gell, Duhl and Giamei (1980)

[6]Dandekar, Martin and Kelley (1981)
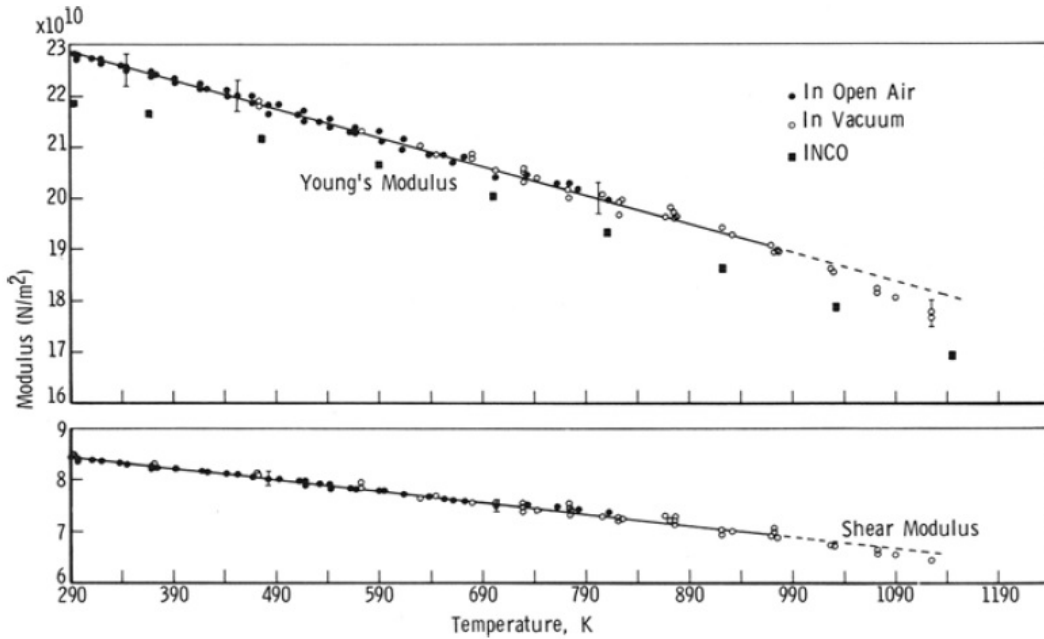
Figure 3.4: Young's Modulus and Shear Modulus over temperature for MAR M200

With regards to the mechanical properties of MAR M200, in "Superalloys: A Technical Guide" by Donachie and Donachie (2002), the ultimate tensile strength and tensile yield strength for the superalloy are tabulated at different temperatures. Those values are shown in Table 3.3.

	Ult. Tensile Strength			Tensile Yield Strength		
	21 °C	538 °C	1093 °C	21 °C	538 °C	1093 °C
	MPa	MPa	MPa	MPa	MPa	MPa
MAR M200	930	945	325	840	880	–

Table 3.3: Mechanical properties of MAR M200

In Table 3.4 and Table 3.5, the major physical properties of the superalloy are shown, like density and thermal properties of the material[7].

---

[7]The mean coefficient of thermal expansion is evaluated from a reference temperature of 22 °C (room temperature).

	Density	Melting Range	Specific Heat		
			21 °C	538 °C	1093 °C
	g/cm^3	°C	J/kg·K	J/kg·K	J/kg·K
MAR M200	8.53	1315-1370	400	420	565

Table 3.4: Physical Properties of MAR M200 (1)

	Thermal Conductivity			Mean Coeff. Thermal Exp.		
	93 °C	538 °C	1093 °C	93 °C	538 °C	1093 °C
	W/m·K	W/m·K	W/m·K	10^{-6} K	10^{-6} K	10^{-6} K
MAR M200	13.0	15.2	29.7	–	13.1	17.0

Table 3.5: Physical Properties of MAR M200 (2)

38

Chapter 4

Turbine Blade Modelling and Instruments Used

The objective of this work has been achieved thanks to the use of a combination of various software and hardware. The steps that made it possible are here elencated, and will later be discussed in more detail.

▶ A JT9D engine first stage turbine blade has been acquired from a collector in Israel;

▶ In the Prototyping Laboratory, located in the Ciri Aeronautica new building, a **preliminary 3D scan** has been realized;

▶ In the Virtual Reality Laboratory, located in the Second Faculty of Engineering and Architecture in Forli, a **more detailed 3D model** has been created;

▶ Then the detailed 3D model was **corrected of the errors** that were produced unavoidably by the 3D scanner;

▶ The final 3D model was imported into a 3D modelling software and then imported again into a **Finite Element Analysis software**;

▶ Inside the FEA software, after defining the properties, the boundary conditions and the loads on the component, **the analysis was carried out** and the results were evaluated.

The following is the list of *software* that were used in the making of the model performed analysis, in order of use:

- ▶ *Roland*'s Dr. Picza;

- ▶ Polygon Editing Tool (PET) from *Konica Minolta*;

- ▶ Rapidform 2011 by *3D Systems*;

- ▶ SolidWorks 2016 by *Dassault Systemes*;

- ▶ ANSYS Workbench 16.0 by *ANSYS*.

And then the *hardware* that was used:

- ▶ JT9D engine scrap first stage turbine blade;

- ▶ Picza Pix-30 Piezoelectric Digitizer from *Roland*;

- ▶ VI-9i (or VIVID-9i) Non Contact 3D Digitizer from *Konica Minolta*.

4.1 Turbine Blade Scanning

The scans of the blade were realized using the Picza Pix-30 Piezoelectric Digitizer, which was connected to a computer that was running the Dr. Picza software. Then the VI-9i Non Contact 3D Digitalizer, connected to a computer with PET and Rapidform installed, was used in order to obtain the final scan.

4.1.1 Picza Pix-30 and Dr. Picza

Figure 4.1: The Picza Pix-30

The Picza Pix-30 is a 3D scanner with Active Piezo Sensor probes which enable very high precision scanning capabilities. It works by making the probe nearly touch the object that is being scanned, creating a 3D model as CAD data. It is mainly used for design or 3D prototyping. It can scan object as large as 30,5 x 20,3 x 6 cm and up to 5kg in weight.

Meanwhile, the Dr. Picza software is easily connected to the machine, allowing easy control over the scans. It is helpful with the scanning as scanning pitch, area and quality can be directly set in the program before the scan even begins; it can also reduce data volume by lowering the resolution of the scan or even rescan the same part (or a particular) for a finer scan, combining it with the previous scans.

4.1.2   VI-9i, PET and Rapidform

Figure 4.2: An example use of the VI-9i

In the Virtual Reality Laboratory, a more detailed scanning technique has been used with the aid of the VI-9i Non Contact 3D Digitizer and the related software.
The VI-9i provides high accuracy 3D measurements of cast, forged and plastic-molded products. It converts the shape of a component into a 3D model in PET by scanning the target with a laser beam; every scan takes approximately 2.5 seconds to complete. Then

the scan can be visualized by the user on the PET software.

Scan after scan, the software is able to merge the different faces (made at different angles), ultimately creating the whole 3D model in 5 to 20 scans, depending on the complexity of the component.

The 3D model is then imported into Rapidform, in which it is better visualized. There, the user is able to see if the merged scans produced any errors, like little holes in the component, for example due to hidden parts that were not picked up by the scans. These types of errors can be easily resolved by Rapidform, creating an accurate model that can be further exported, allowing major changes in the model or analyses to be readily conducted on it.

4.2 SolidWorks and ANSYS

After the 3D model was created with contact and non contact technologies, it can be exported to a more specific 3D modeler, like SolidWorks, which is a computer aided design (CAD) solid modeling software, and a new version is published by *Dassault Systemes* every year. The file extension produced by Rapidform is fully compatible with a software like SolidWorks.

In Solidworks, the 3D model previously created can be described only as a "shadow" of the scanned component, meaning it has not a solid form, but, thanks to various functions inside the software it is possible to recreate the solid model based on the imported shadow, ultimately giving it a solid structure.

After the solid model is completed, it is possible to import it, thanks to an integrated feature in SolidWorks, inside the ANSYS Workbench environment, which is a part of the ANSYS software package. ANSYS is a computer aided engineering (CAE) software that uses Finite Element simulations in order to compute structural and thermal analyses, fluid dynamics around a body and much more.

4.2.1 Finite Element Analysis

A Finite Element Analysis (FEA) is a numerical computer technique used for engineering analyses. The technique finds approximate solutions for partial differential equations by subdiving a large and complex problem into smaller and simpler parts in order to solve it computationally. Aside from representing a complex geometry in a more accurate manner,

this tecnique also allows to point out any local effects that could be present (like a local mechanical stress).

Analysis Process

In ANSYS, like in most of the commercial FEA softwares available, the analysis process is made of three steps:

▶ **Pre-processing**, where the finite element model is defined: choice of the type of analysis, definition of the engineering parameters of the material, mesh creation, application of loads and boundary conditions, etc.;

▶ **Processing**, where the problem is solved by the software;

▶ **Post-processing**, where the obtained solution is elaborated and presented to the user thanks to a user-friendly interface.

4.3 Turbine Blade Modelling

Now that all the tools and instruments that have been used for the realization of this work have been cited and briefly presented, the actual tasks that were performed will be presented in more detail, with the help of imagery as well.

First of all, as already mentioned, the scrap turbine blade was acquired from a collector located in Israel. The blade, due to its long operative life, presents light signs of consumption of the MAR M200 alloy of which it is composed. The holes assigned to create the protective cooling film are visible, alongside some signs of corrosion around some of them. In Figure 4.3, two different shots of the blade are presented. In these pictures, it is evident how some parts have been more subjected to thermal stress rather than others, as the clearer parts have been more protected from high temperature gradients thanks to the cooling film that was much more intense in those areas of the blade.

4.3.1 The First Two Scans

The first two scans were realized by the Picza Pix-30 and the related Dr. Picza software. For the first scan, the turbine blade was laid face down (pressure surface down) on the 3D scanner. Then the blade was flipped (suction face down) and another scan was made.

Figure 4.3: Front and back views of the turbine blade

Every scan took around 8 hours to complete, so a couple of days were required for this first stage of the project.

4.3.2 Creation of a Finer Model

After this stage, in the following days, with the help of the VI-9i Non Contact 3D Digitizer, the Polygon Editing Tool and Rapidform, a finer overall scan of the blade was made. Laser scanning, in contrast with the Pix-30, produces much more quickly the desired scan (order of seconds), but needs more attention by the user first in the setup and then in the merging process. The Pix-30, after a quick setup of the scanning area that took just a couple of minutes, was able to independently work without any input from the user; meanwhile the scanning technique with the VI-9i needed much more attention in the setup process (the main factors that cause this are the bulkiness of the equiment, all the cable that needed to be correcly attached to the machine and the fact that the VI-9i needed to reach its operating temperature before any scan could be done).

After the initial setup was completed, a series of scans were realized; twenty to be more precise. At every scan the focus needed to be adjusted in order to compensate for

Figure 4.4: The VI-9i during one of the scans of the turbine blade (on the right)

movement of the "blade-boxes" system at every blade change of angle made. A photo was taken during one of the scans and is presented in Figure 4.4 as a visualization of the process.

Every new scan had to be merged with the one that preceded, and this was done thanks to the PET software, that uses a very clear interface to do so. In order to be effectively merged, the two scans needed three reference points, or surfaces, to make the program able to recognize said surfaces and overlapping the adiacent scans. By doing so, scan after scan, the complete 3D model was constructed by the software. But, due to the smallness of the component and the fact that it was sitting on carton boxes all the time to stabilize it, a few errors were picked up by the various scans, and the user was able to remove most of them directly in the PET interface. A partial representation of the process can be seen in Figure 4.5, alongside some of the unwanted parts, which appear to be randomly floating around in the merged scans.
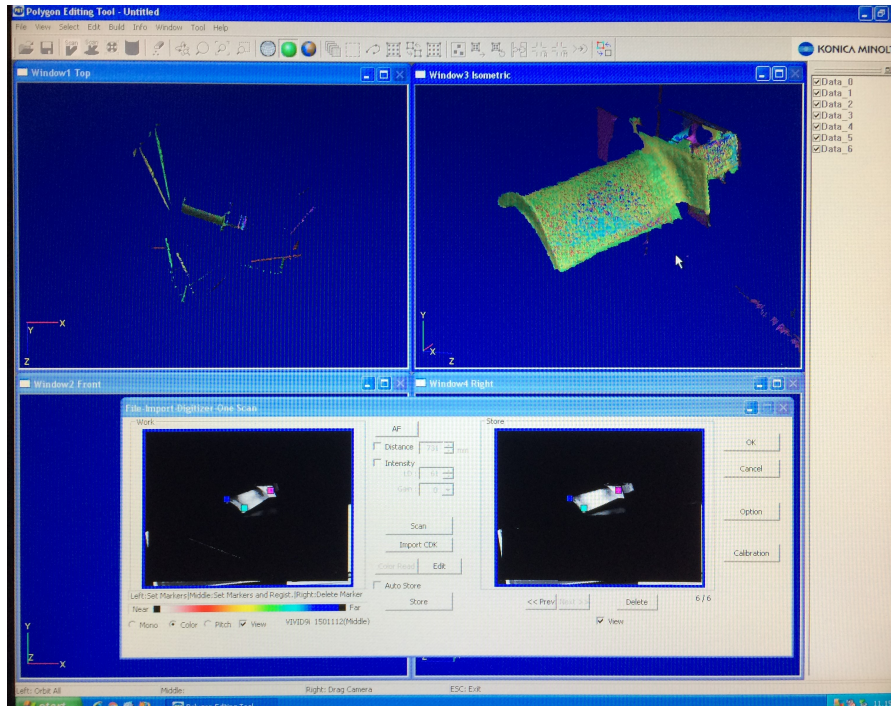
Figure 4.5: PET interface and partial creation of the blade model (made during two scans)

After patiently creating the surface model of the component in PET, it could be imported into Rapidform for further refinement and error correction. In Rapidform, the "floating" parts of the scans were removed. Then the program was able to detect any imperfections in the meshed model, like holes at points in which the scan did not pick up any material, even if there was, and *abnormal faces*. These errors could be attributed mainly to human error, as the VI-9i is accurate to μm, to lighting or other environmental factors. These mesh holes are easily fixable thanks to the many tools available to the user in Rapidform. After the error correction phase, a model refinement phase was conducted, in which the mesh was further molded in order to better represent how the component looks like in real life.

The final model produced by Rapidform is presented in Figure 4.6.

4.3.3 Model Implementation in SolidWorks

After the final blade model was created in Rapidform, the created file was readily available to be opened in SolidWorks as a mesh file. The model is the SolidWorks environment is shown in Figure 4.7. But, as already mentioned, the imported mesh can be described as a "shadow" of the turbine blade. In order to give solidity to the model two SolidWorks functions were used: the *spline* and the *loft* functions. The first one allows to create
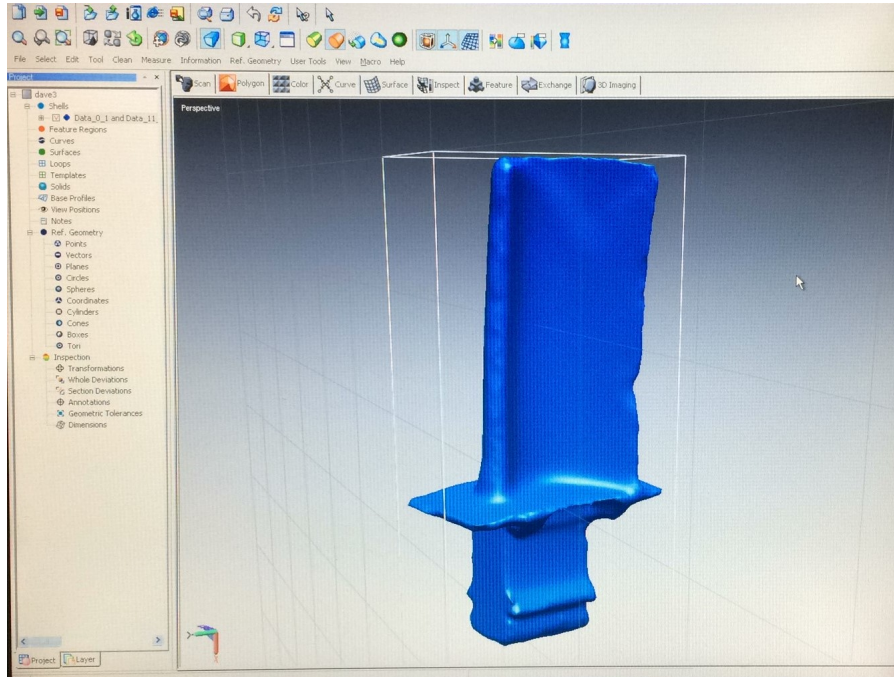
Figure 4.6: Final blade model in Rapidform
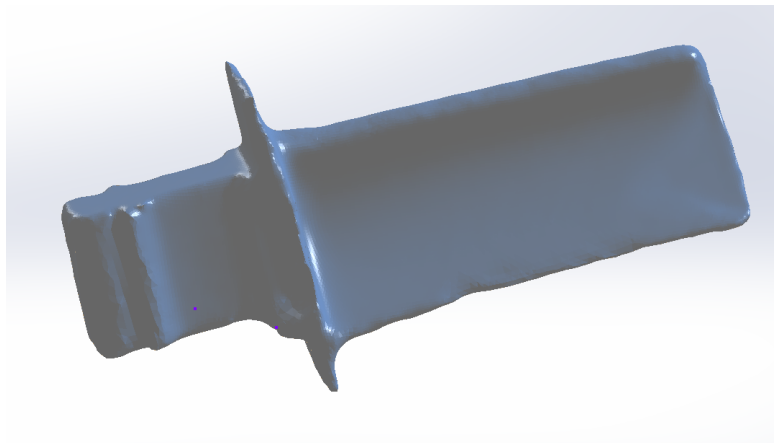
Figure 4.7: Blade model in SolidWorks

splines on a predefined plane around the border of the blade model, creating the cross section of the blade at that point; this has been done ten times, as shown in Figure 4.8. Then the loft function allowed to recreate the blade with the splines as references.

The main part of the blade was then created thanks to these exploits.

The same process was not done with the base, as the interest of this work was to analyse only the blade part. In all the computations, at the base, a fixed support has been introduced as a boundary condition. So the base was simplified as a blunt parallelepiped. The final 3D model that has been used in all the analyses of this work is shown in Figure 4.9.
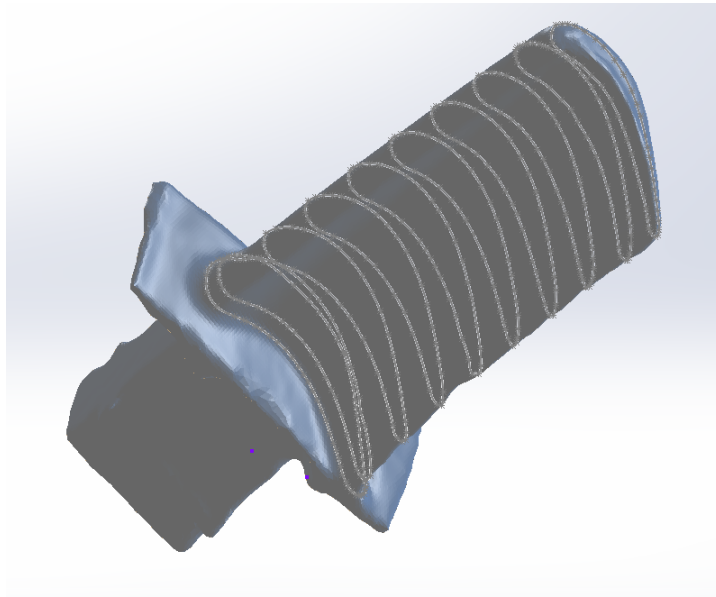
Figure 4.8: Splines around the model

Figure 4.9: Final SolidWorks model

Chapter 5

MAR M200 First Stage Turbine Blade Analysis

In this chapter, after the extensive theoretical background given, the finite element analyses have been carried out.

The analyses were conducted with a powerful finite element analysis commercial software called ANSYS, developed by *ANSYS*, more precisely in the ANSYS Workbench environment.

In the following pages, a comprehensive explanation of the steps that were required to conduct these analyses will be given.

The first one was a *Static Structural* analysis, in which the most relevant mechanical stresses on the turbine blade were simulated. The results are clearly shown thanks to a very user-friendly interface which uses different colors for different final results.

Subsequently, a *Transient Thermal* analysis was conducted on the same geometry. In this case, the extreme thermal conditions to which the blade is subjected due to its positioning in the engine were simulated, and the results were also clearly shown in the interface.

The given final results were found to be in accordance with simulations that were conducted on similar geometries and environments.

5.1 Preliminary Stage

The first part of the set-up for both analyses consisted in the definition of the geometry and the material that were used.

In the first interface of the Workbench environment, a Project Schematic is shown, after selecting the two different types of analyses, as shown in Figure 5.1. In this schematic, all the required steps are summarized.
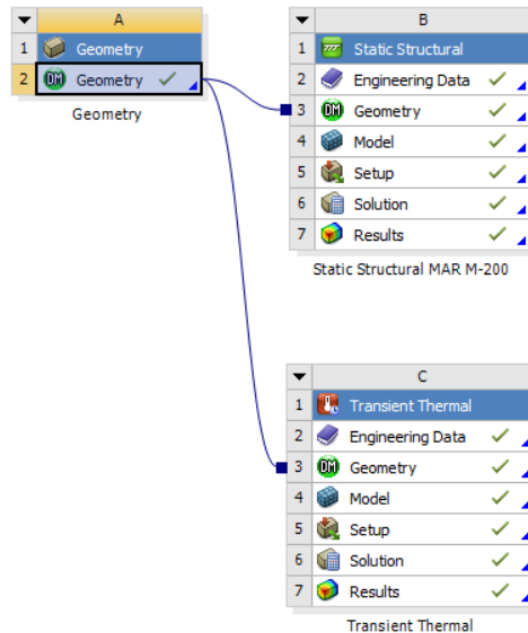
Figure 5.1: Project Schematic in the Workbench environment

As seen in Section 4.3, the geometry was imported directly from SolidWorks, thanks to its "Export to ANSYS" function. It was then opened in the DesignModeler inside of ANSYS, in which the proper solid model was created by ANSYS for the following required computations, as seen in Figure 5.2. The dimensions and the main properties of the model

ares shown in table 5.1.

	Turbine Blade Model
Length X	41 mm
Length Y	23,35 mm
Length Z	76 mm
Volume	25443 mm^2
Mass	0,22 kg

Table 5.1: Main model characteristics

Then, in the Engineering Data tab, all the information about the MAR M200 material was added into ANSYS. This information includes various mechanical and thermal properties of the superalloy, as shown in Section 3.3: density, isotropic elasticity, mean coefficient of thermal expansion, tensile ultimate strength, specific heat and thermal conductivity were inserted into the calculations. These material characteristics were used in all the analyses.
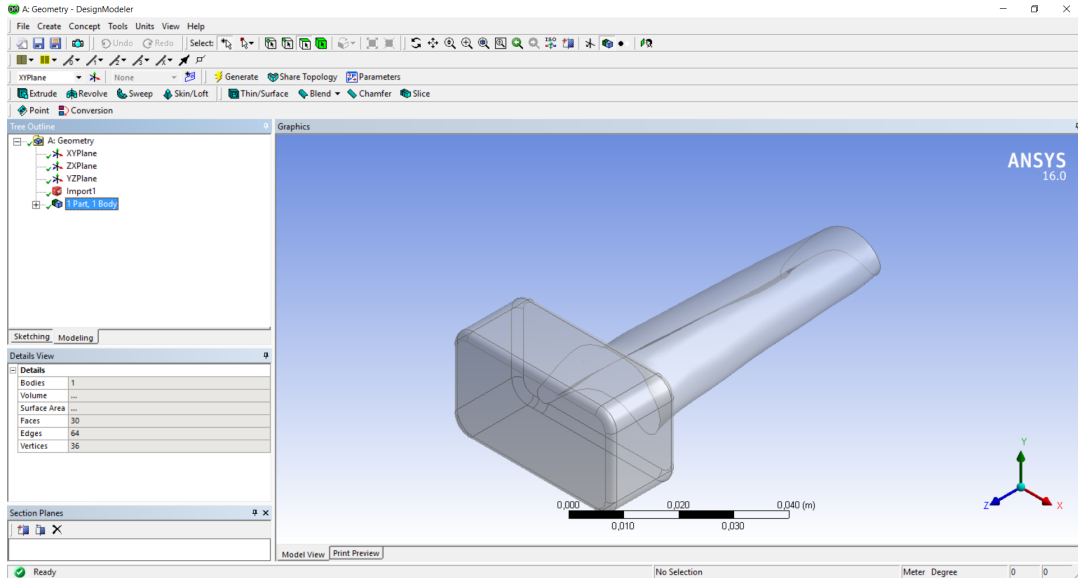
Figure 5.2: Blade model in the DesignModeler interface
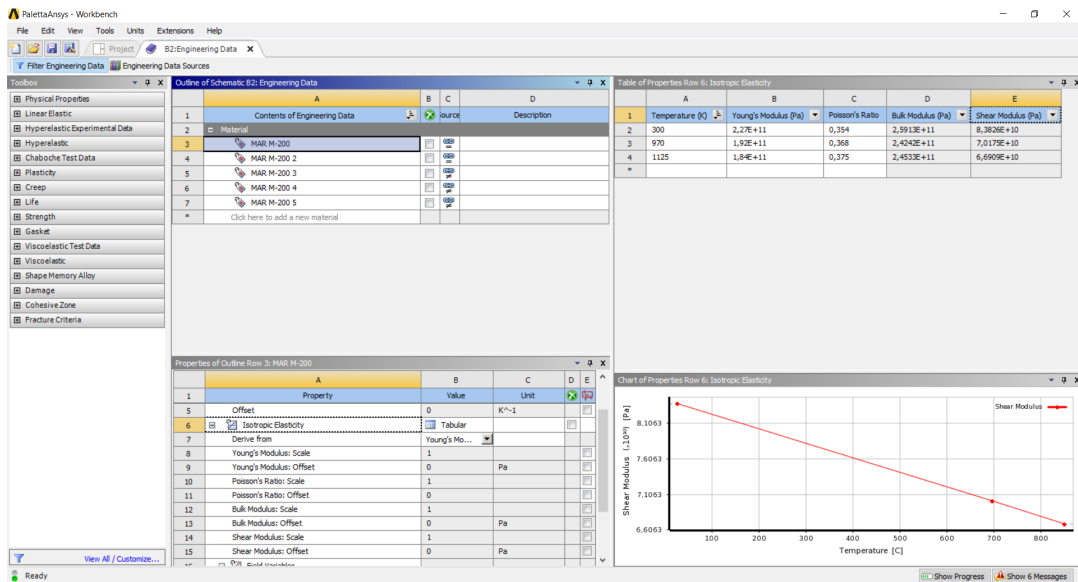
Figure 5.3: The Engineering Data interface

5.1.1   Mesh Definition

After defining the geometry, it is now possible to create a mesh in the "Model" tab. It opens up a new interface, the ANSYS Mechanical interface.

The mesh was easily generated with ANSYS default settings for meshing, but some sizing options were changed: the sizing function was set to *curvature* to create a more precise mesh around curved elements; also the relevance center was set to *medium*. The mesh although was not as detailed as it was needed to be. So for three faces of the turbine blade model a finer face sizing (it is to be reminded that the elements are triangular shaped): the elements of the blade tip, the blade itself and its base were meshed with a 1,5 mm element size, resulting in a much finer mesh for these faces. Also, a level 1 *refinement* for these three faces was added, for further meshing precision. This was done as those parts are the most subjected to stresses, requiring finer and more precise calculations.

The final result is shown in figure 5.4.
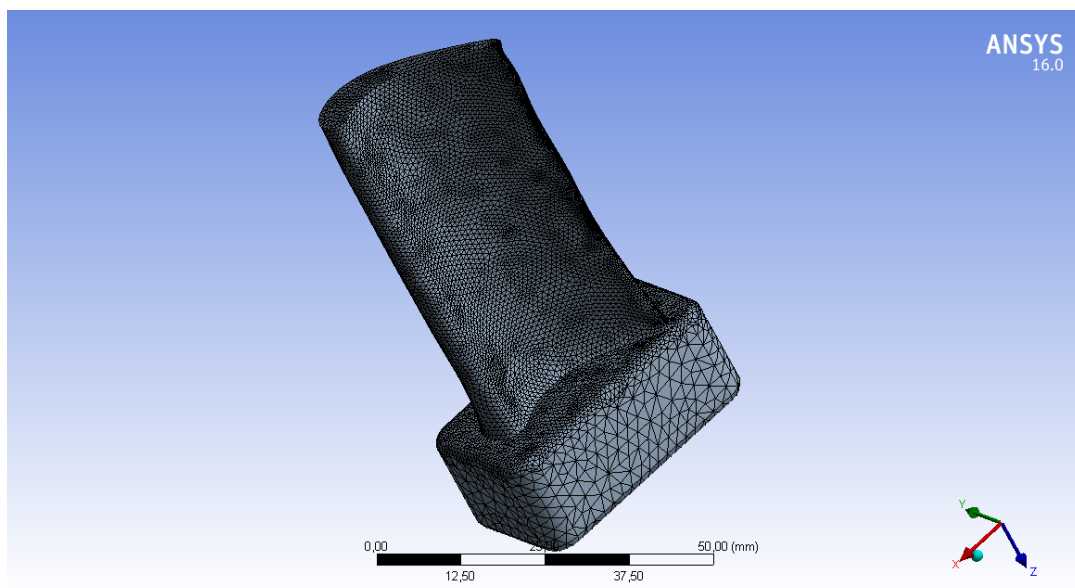
Figure 5.4: Final mesh of the blade

The final mesh resulted in the creation of 76445 nodes and 37249 elements throughout the model.

5.2 Static Structural Analysis

In this section, the focus will be on the steps regarding the Static Structural finite analysis of the blade. After the preliminary stage which was common between the two analyses, in the static structural interface the mechanical loads on the blade were simulated and the most relevant results were evaluated.

5.2.1 Setup Stage

In this phase, while in the Mechanical interface, it was possible to add loads and boundary conditions to the model in order to simulate the rotation of the blade while it is operating inside the engine, thus calculating the minimum and maximum stresses to which it is subjected under these loads.

Centrifugal Force

As already mentioned multiple times throughout this work, the main source of mechanical stress in a rotating turbine blade are due to *centrifugal forces*, induced by the high speed rotation of the engine.

Using the available data, the centrifugal force and acceleration were calculated using the following equation:

$$F_c = m\omega^2 r \tag{5.1}$$

where m is the mass of the body involved (in kilograms), ω is the rotational velocity (in RPM, rounds per minute) and r is the radius (in meters).

First of all, the *real* component used for the analyses weighted approximately 150 grams, as it was possible to weight it. It differs from the mass shown in Table 5.1 as the base was crafted during the creation of the model as an approximation, and it is not representative of the real base of the blade.

Meanwhile, from the literature[1], it was possible to know what the rotational velocity was. For a JT9D-7A turbofan engine, in which the blade was mounted, the rotational velocity of the HPT had a maximum operating value of 8000 RPM, which equals to a linear velocity of approximately 394 m/s(while the LPT had a maximum operating value of 3750 RPM).

---

[1]Pratt & Whitney, *Type Certificate Data Sheet E20EA, Revision 14*, 10 February 2000

Also from specifications of the engine, it was possible to obtain the diameter of the first turbine stage, which was ~ 94.1 cm, therefore the radius used for the calculations was 47.05 cm.

The resulting force amounted to 49532 N.

The centrifugal acceleration was also calculated (and later simulated in the analysis) and amounted to **33637 g**, a value in accordance with the literature[2].

After calculating the acceleration, in order to simulate it inside ANSYS, it was converted from g to m/s^2.

$$a_c = 33637 \; g \approx 329866 \; \frac{m}{s^2}$$

Then, as boundary condition, it was introduced in the analysis as a ramped acceleration with an outwards direction, as shown in Figure 5.5.
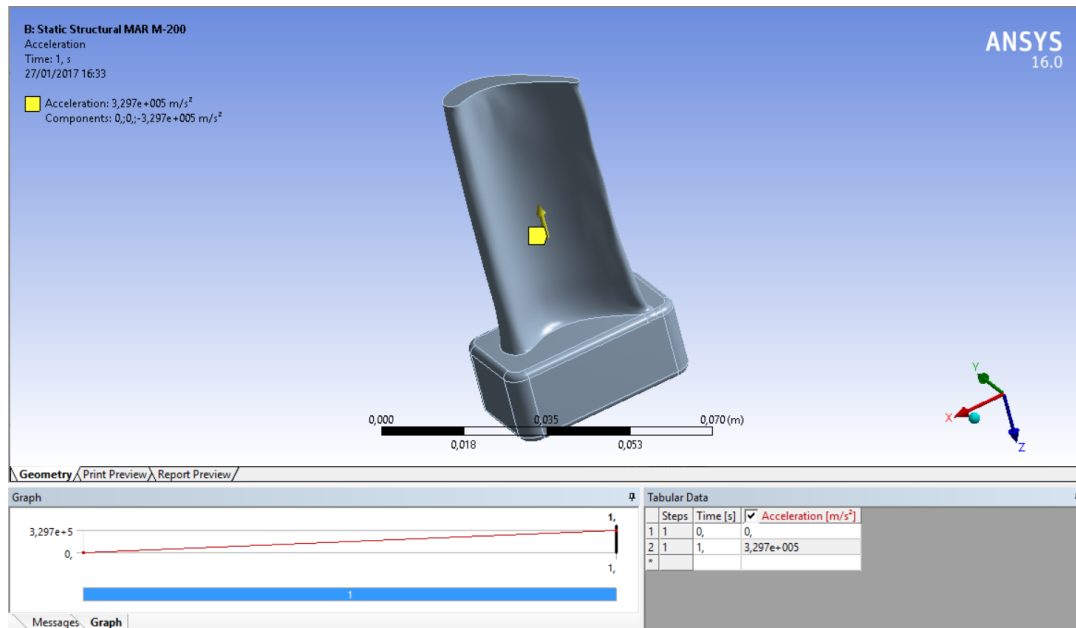
Figure 5.5: Ramped centrifugal acceleration applied on the model

It is to be noted how the implemented acceleration value is in the **worst operating condition** of the engine, as the maximum rounds per minute allowed (by the designers definition) were used.

---

[2]Mattingly, Heiser and Pratt (2002)

Fixed Support

As another boundary condition, a fixed support has been included in the Mechanical interface, as shown in Figure 5.6.
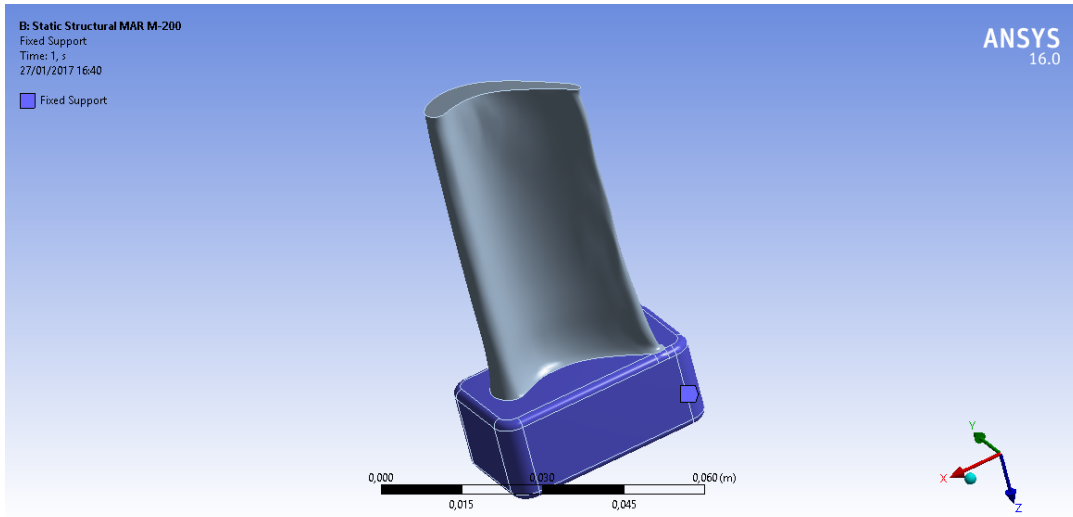
Figure 5.6: Fixed support on the base of the blade

The fixed support includes all 28 faces of the base (represented as a blunt parallelepiped), which was simplified compared to the real base of the blade, as it would not have had much influence on the output of the analysis.

Step Control

For further precision of results, in the analysis settings tab, 8 substeps in the analysis have been set, meaning that during the analysis, 8 different output values were evaluated and tabulated by ANSYS for each individual wanted result.

Awareness of Simplifications in the Analysis

To simplify the analysis, which is to be reminded is a *preliminary* structural analysis, some factors have been omitted, and therefore left out. As it is a simplified model, only the most influencial stress-inducing factor has been included, that is, the centrifugal acceleration. So, structural stresses present in the real operative environment of the blade, such as thermal and air pressure inducing stresses were not considered in this preliminary analysis.

56

5.3   Static Structural Analysis Results

After introducing all the conditions for the analysis, three main results have been evaluated: **Equivalent Von-Mises stress** across the blade, **Total Deformation** and **Equivalent Total Strain**.

5.3.1   Equivalent Stress

The final equivalent stress distribution across the blade is shown in Figure 5.7. The first image is of the rear the blade, while the second is of the front.
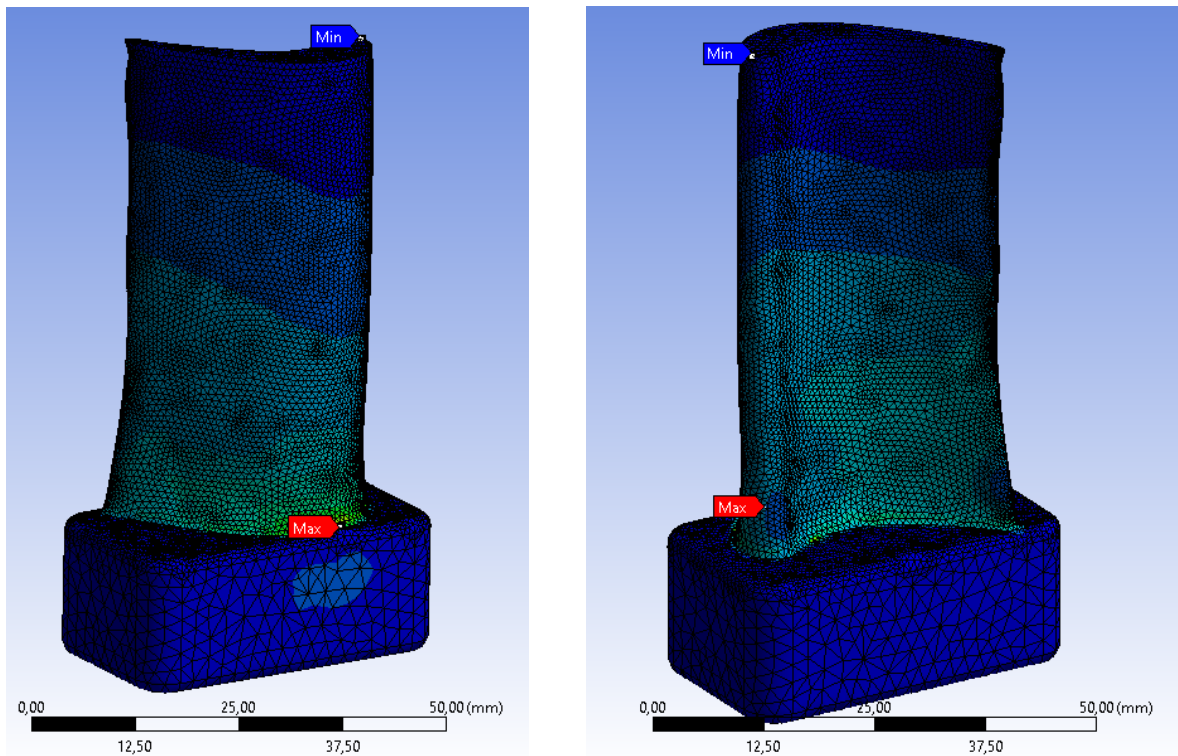
Figure 5.7: Equivalent stress distribution across the meshed blade

In the above pictures, points where the minimum and maximum stresses occur are clearly indicated. The hotter colours represent a higher stress distribution, while colder colours represent the areas where the distribution of stress is lower or even non-existent.
In Figure 5.8, the stress values allocated for each colour are gradually shown from highest to lowest (in MPa).
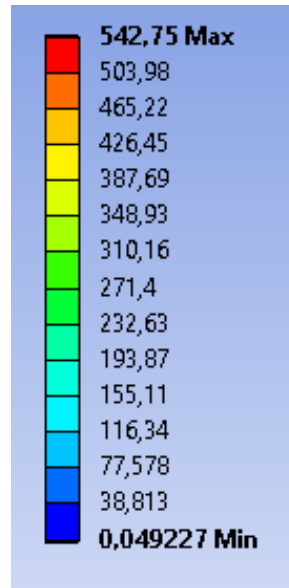
Figure 5.8: Stress values (MPa) and respective colours

In Figure 5.9, a more detailed image of the area in which the stress is at its maximum is shown. In this case the mesh has been removed for clarity.
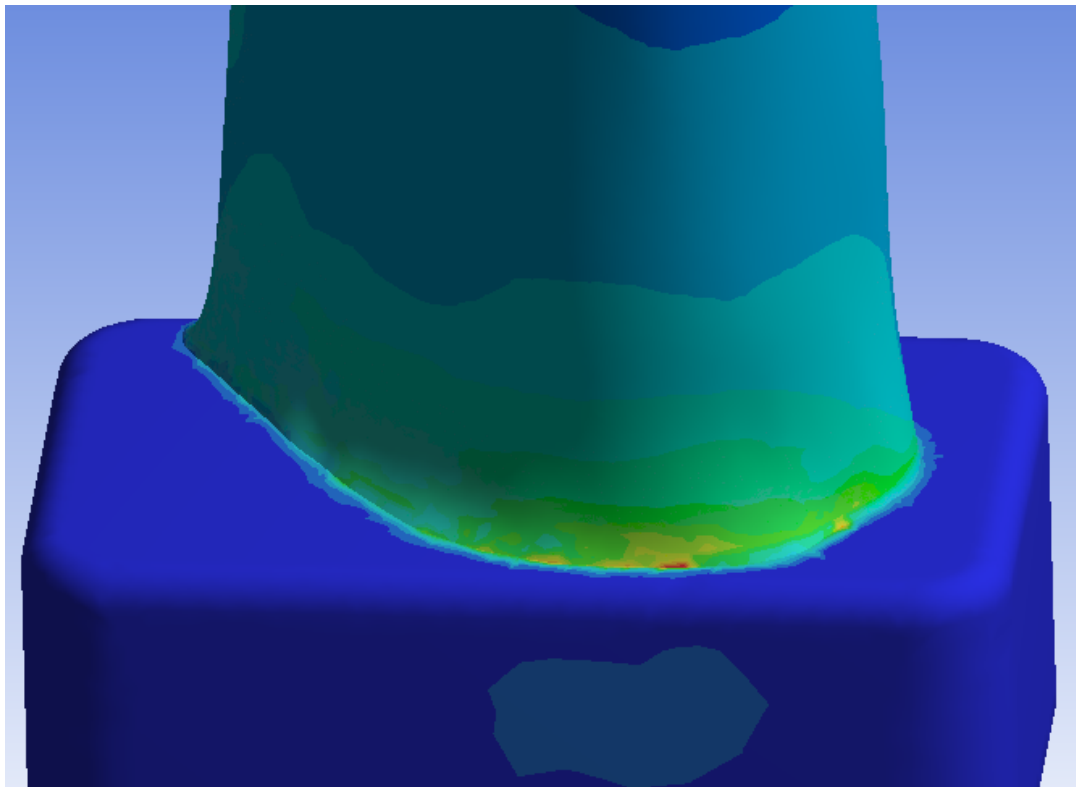
Figure 5.9: Detail of the most stressed area of the blade

On the opposite, in Figure 5.10 a more detailed image of the blade tip is shown. On the tip area, the least amount of stress is present.
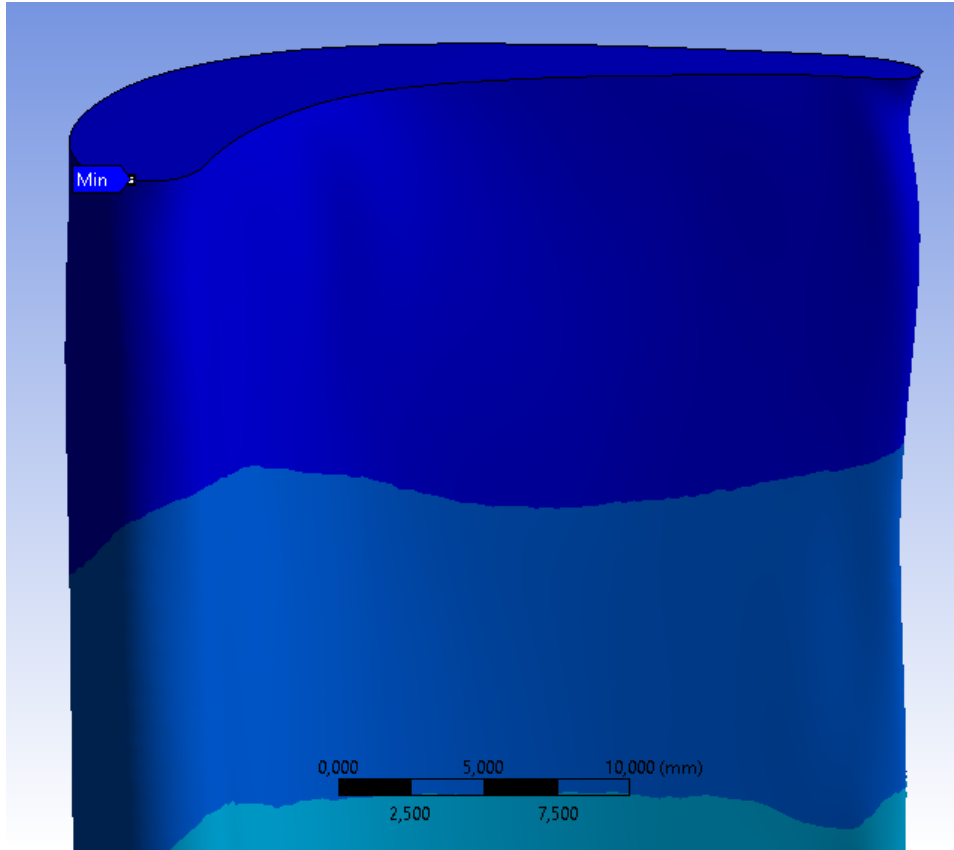
Figure 5.10: Detail of the least stressed area of the blade

It is clear that, in this analysis, with the applied boundary conditions, the most solicited part of the whole blade is the blade **attachment to the base**, while the least one is on the **tip** of the blade.

A summary of the most relevant results of the equivalent stress distribution is shown in Table 5.2.

	Stress Value	Location
Maximum	542.75 MPa	Blade attachment to the base
Minimum	0.049 MPa	Blade tip

Table 5.2: Summary of main results of the equivalent stress distribution

5.3.2 Total Deformation

The total deformation of the blade under the assigned conditions is shown, in millimeters, in Figure 5.11.
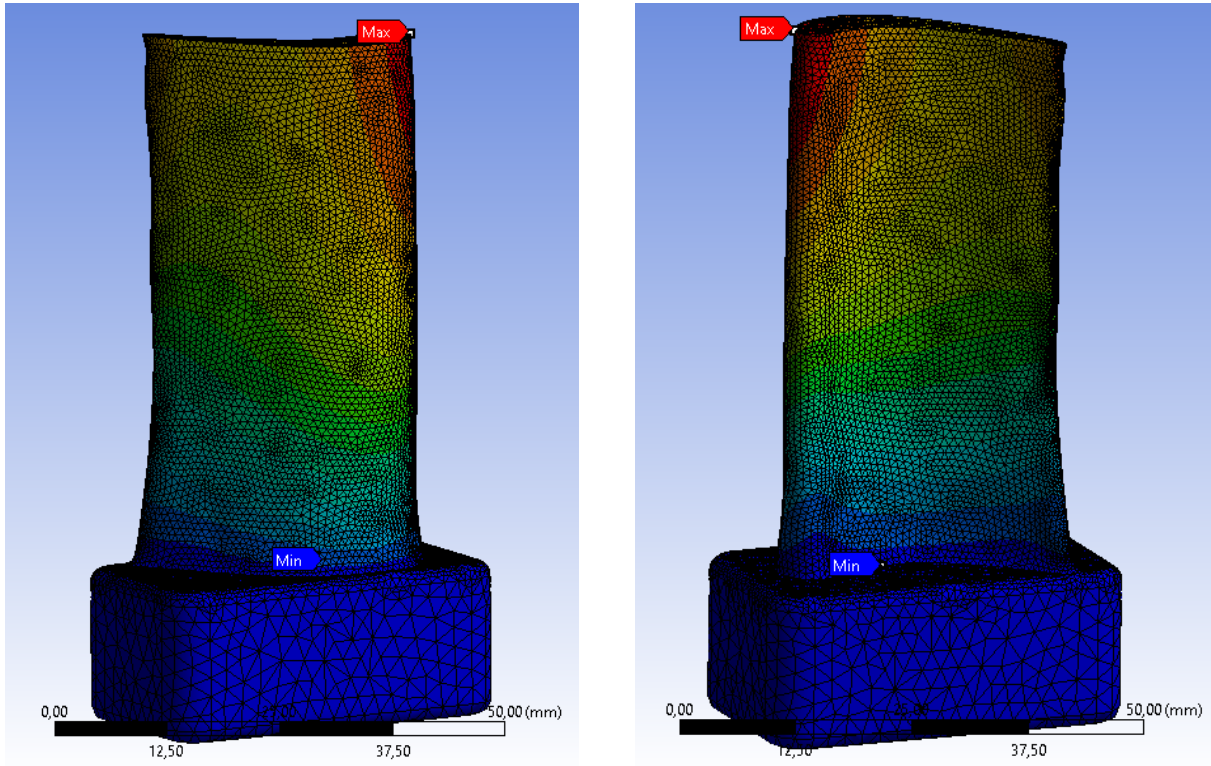
Figure 5.11: Total deformation of the meshed blade
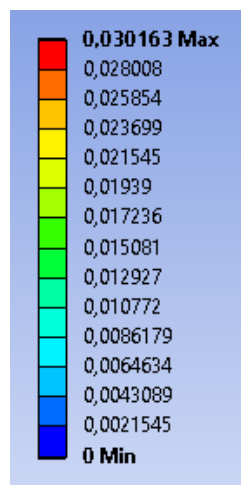
Figure 5.12: Total deformation values (mm) and respective colours

Much like in the previous results, in Figure 5.12 the colours associated with the different deformations are shown.

In this results it is to be noted that the maximum deformation of the blade is located on the **area of the leading and trailing edges** of the blade tip, while the attachment to the base is **practically undeformed**.

In Figure 5.13 a more detailed (meshless) image of the blade tip is shown for clarity.
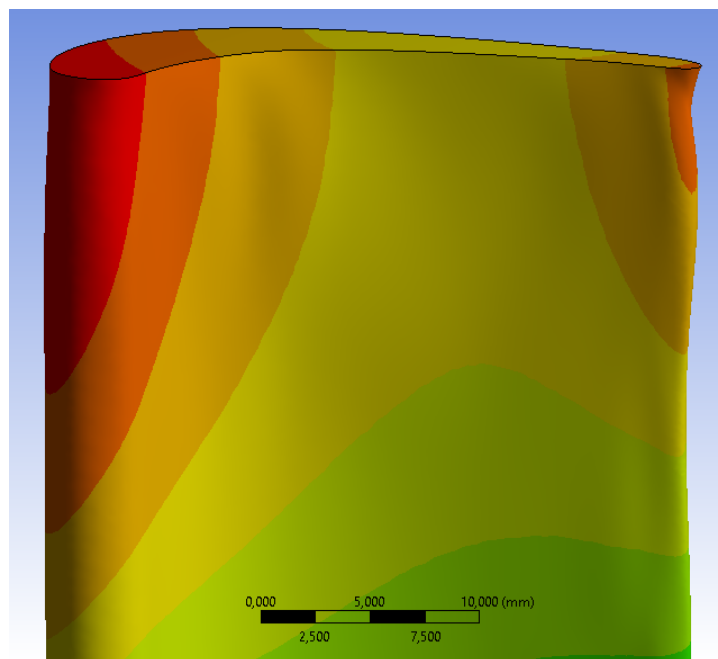
Figure 5.13: Detail of the total deformation on the blade tip

A summary of the total deformation is shown in Table 5.3.

	Deformation	Location
Maximum	0.0302 mm	Leading edge of the blade tip
Minimum	0 mm	Base and lower part of the blade

Table 5.3: Summary of main results of the total deformation

5.3.3 Equivalent Total Strain

Next, the equivalent total strain has been evaluated. The results are shown in Figure 5.14.
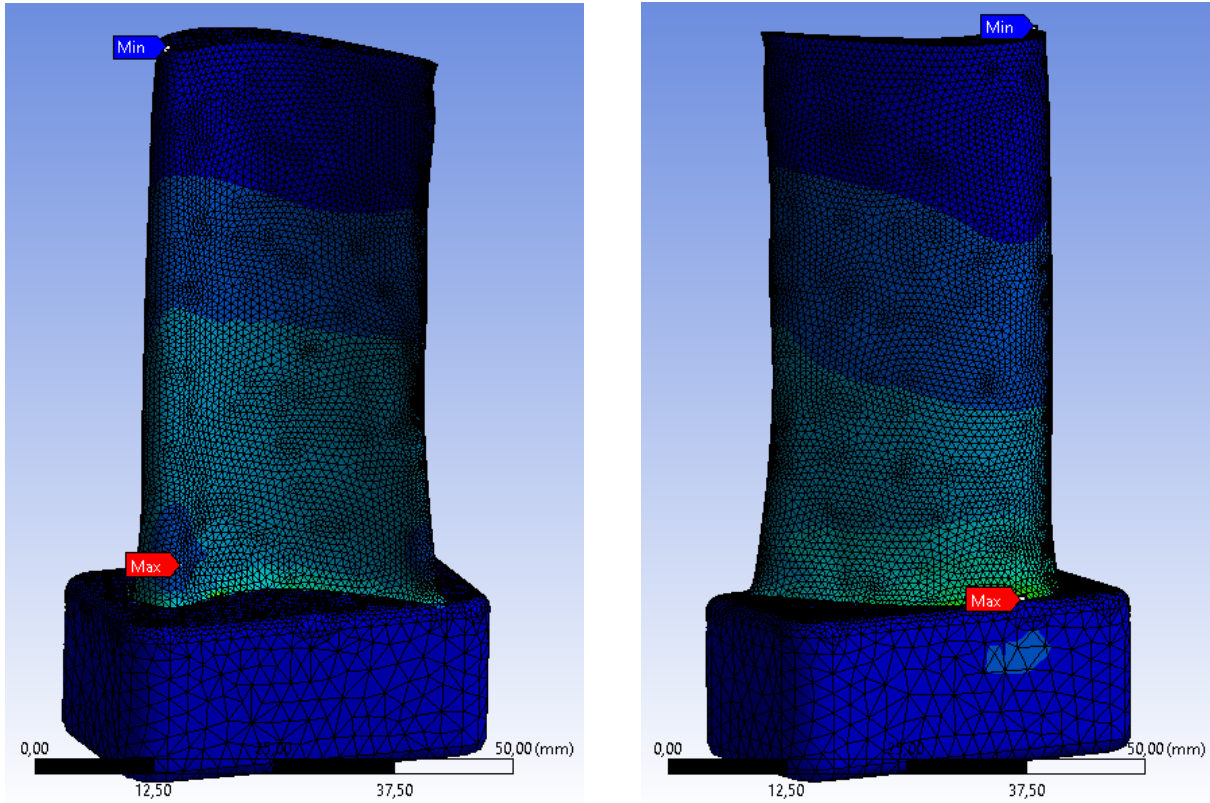
Figure 5.14: Equivalent total strain distribution on the meshed blade
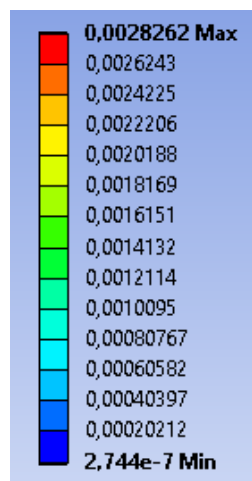
Figure 5.15: Equivalent total strain values (mm/mm) and respective colours

The equivalent total strain maximum and minimum values are positioned roughly in the same areas of the corrispondent values of equivalent Von-Mises stress.

A summary of the maximum and minimum values and its positions can be found in Table 5.4.

	Equivalent total strain	Location
Maximum	0.0028 mm/mm	Blade attachment to the base
Minimum	$2.74 \cdot 10^{-7}$ mm/mm	Blade tip

Table 5.4: Summary of main results of the equivalent total strain distribution

5.3.4 Tabulation and Graphical Representation of Results

In this section, table of all the results of the analysis given by the implementation of the substeps will be shown.

Equivalent Stress

Time (s)	0.125	0.25	0.375	0.5	0.625	0.75	0.875	1
Max Stress (MPa)	67.843	135.69	203.53	271.37	339.22	407.06	474.9	542.75

Table 5.5: Maximum equivalent stress over time

Equivalent Total Strain

Time (s)	0.125	0.25	0.375	0.5	0.625	0.75	0.875	1
Max Strain (mm/mm)	$3.53 \cdot 10^{-4}$	$7.07 \cdot 10^{-4}$	$1.06 \cdot 10^{-3}$	$1.41 \cdot 10^{-3}$	$1.77 \cdot 10^{-3}$	$2.12 \cdot 10^{-3}$	$2.47 \cdot 10^{-3}$	$2.83 \cdot 10^{-3}$

Table 5.6: Maximum equivalent total strain over time

Stress-Strain Graph
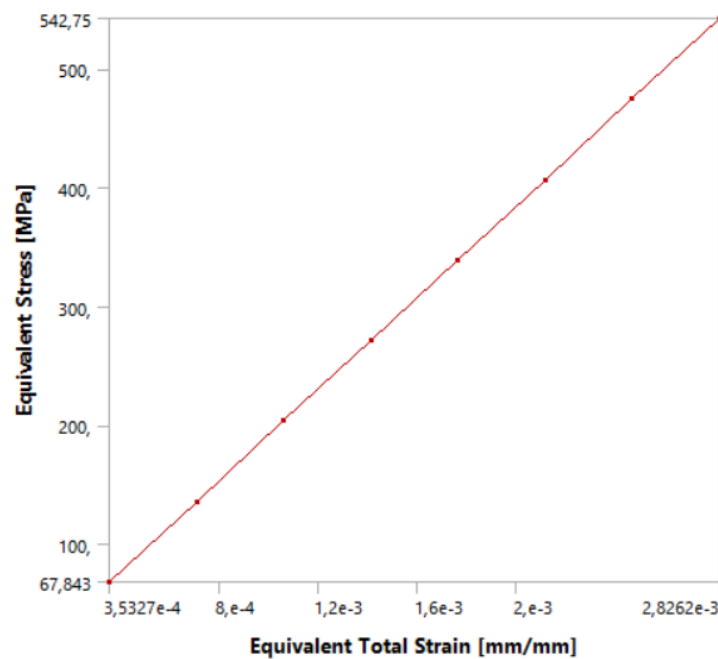
Figure 5.16: Stress-Strain graph from the results of the analysis

5.4   Transient Thermal Analysis

With regards to the transient thermal analysis, the geometry and the mesh were the same as the ones used in the previous static structural analysis. Of course, the engineering data was the same as well, sharing the MAR M-200 material properties as before.

A difference between the analyses can be found in the analysis settings: instead of 8 substeps, values at 17 substeps were evaluated, giving more results throughout the process than in the previous one.

5.4.1   Setup Stage

First of all, in order to perform this type of analysis, the user is required to set an initial *uniform temperature*. It was set to room temperature, or 22 °C.

Convection

The main input for this type of analysis is *convection*. The software requires a *surface* over which evaluate the results of the convection, a *ramped ambient temperature* and the *film coefficient* (or heat transfer coefficient) of the fluid sorrounding the blade.

The film coefficient is defined as follows:

$$h = \frac{q}{\Delta T} \qquad [W/m^2 \cdot K] \qquad (5.2)$$

where q is the heat flux, or the thermal power per unit area, and ΔT is the temperature difference.

The surface of the blade was selected, as shown in Figure 5.17. Meanwhile, a constant ambient temperature of 750 °C was set, which is nearly the maximum operative temperature set by the designers for the JT9D-7A propulsion unit. The film coefficient was set to 100 W/m²·K, which is a typical value for hot air.
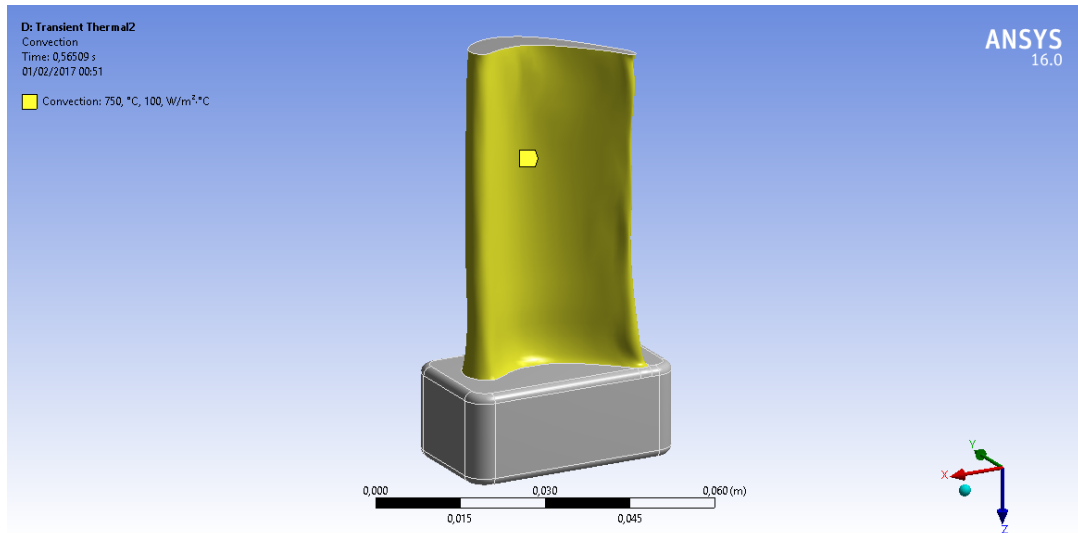
Figure 5.17: Surface of the blade to which convection is applied

5.5 Transient Thermal Analysis Results

For this analysis, two results were evaluated: **Temperature** distribution across the blade and **Total Heat Flux**.

5.5.1 Temperature
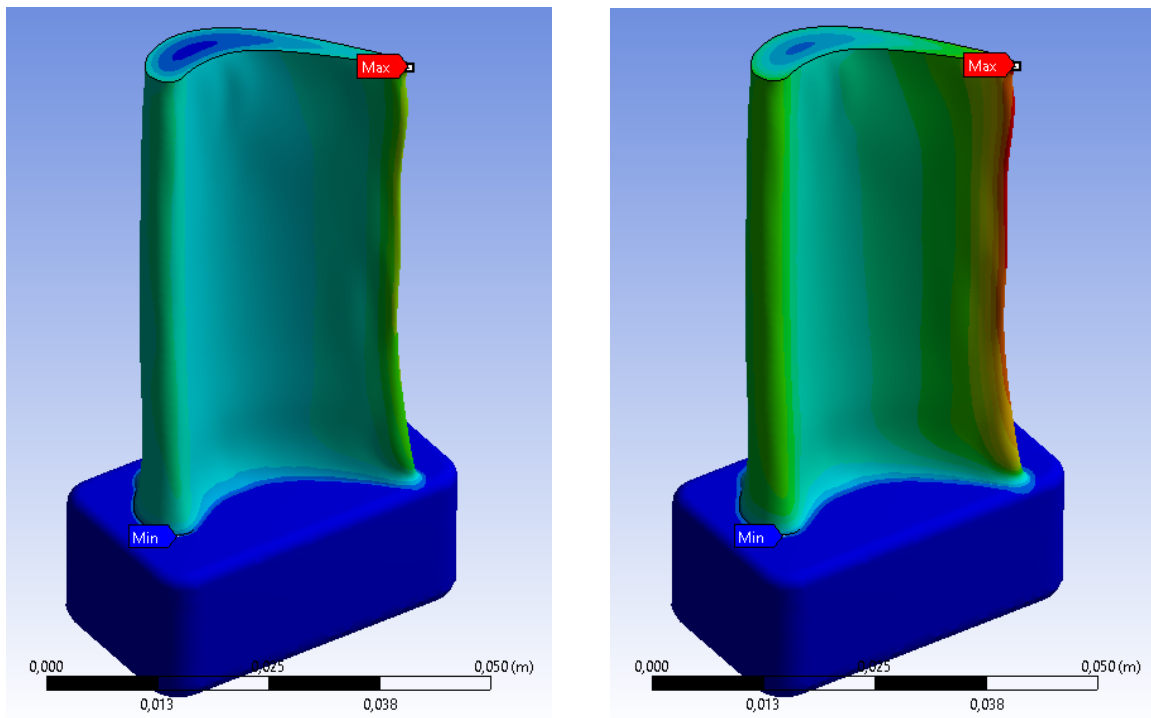
Figure 5.18: Blade front temperature distribution at 0.5 s and at the end of the analysis
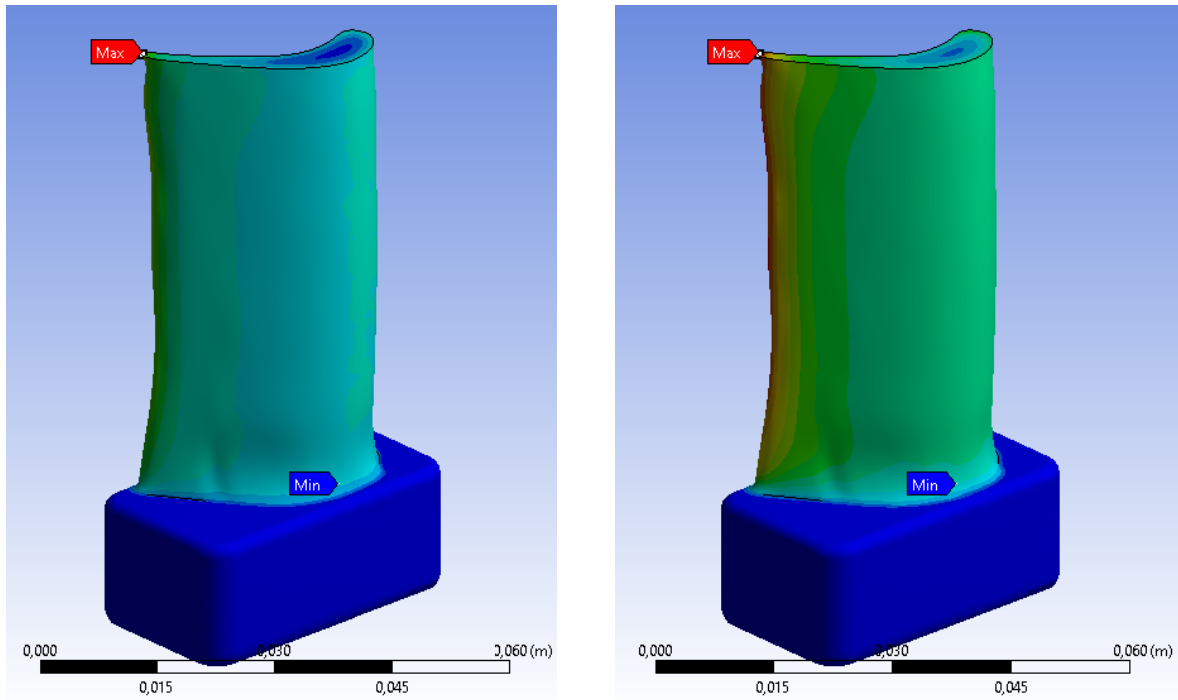
Figure 5.19: Blade rear temperature distribution at 0.5 s and at the end of the analysis
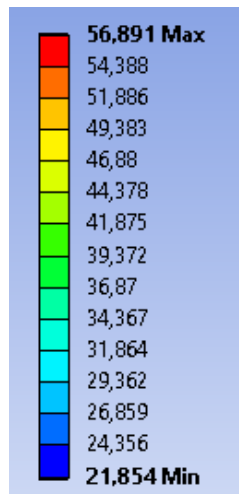
Figure 5.20: Temperature values (°C) and respective colours

As seen in the above Figure 5.18 and Figure 5.19, after one second of analysis, the hotter part of the model is the blade **trailing edge**, reaching its maximum at the tip (56.89 °C). It is to be noted how, over time, some parts of the component heat up, gradually: first the leading edge; then hotter temperatures spread across the blade surface and inside of the blade itself. The sections with more material tend to heat up more slowly than ones with less material (a prime example is the trailing edge itself).

67

In Table 5.7, all the results of maximum temperature values throughout the 17 substeps are shown over time.

Time (s)	Temperature (°C)	Time (s)	Temperature (°C)
0.03	25.407	0.48	42.784
0.06	27.001	0.55	44.756
0.08	28.339	0.61	46.668
0.15	31.332	0.68	48.53
0.21	33.96	0.75	50.349
0.28	36.362	0.81	52.125
0.35	38.609	0.88	53.868
0.41	40.741	0.95	55.58
	Continues...	1	56.981

Table 5.7: Maximum temperature values over time
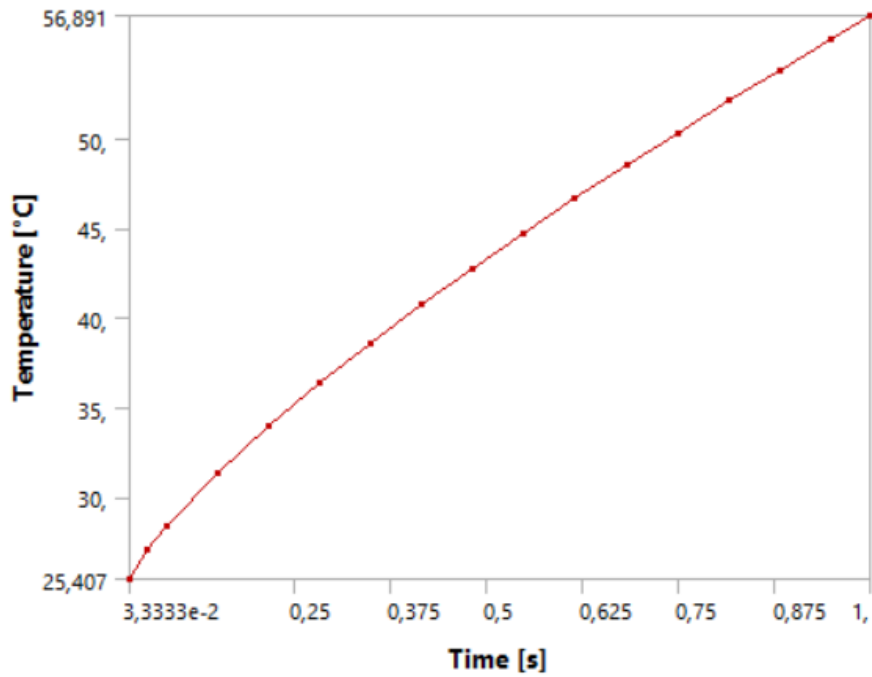
Figure 5.21: Temperature over time graph

5.5.2   Total Heat Flux

The following results shown the total heat flux distribution across the model.
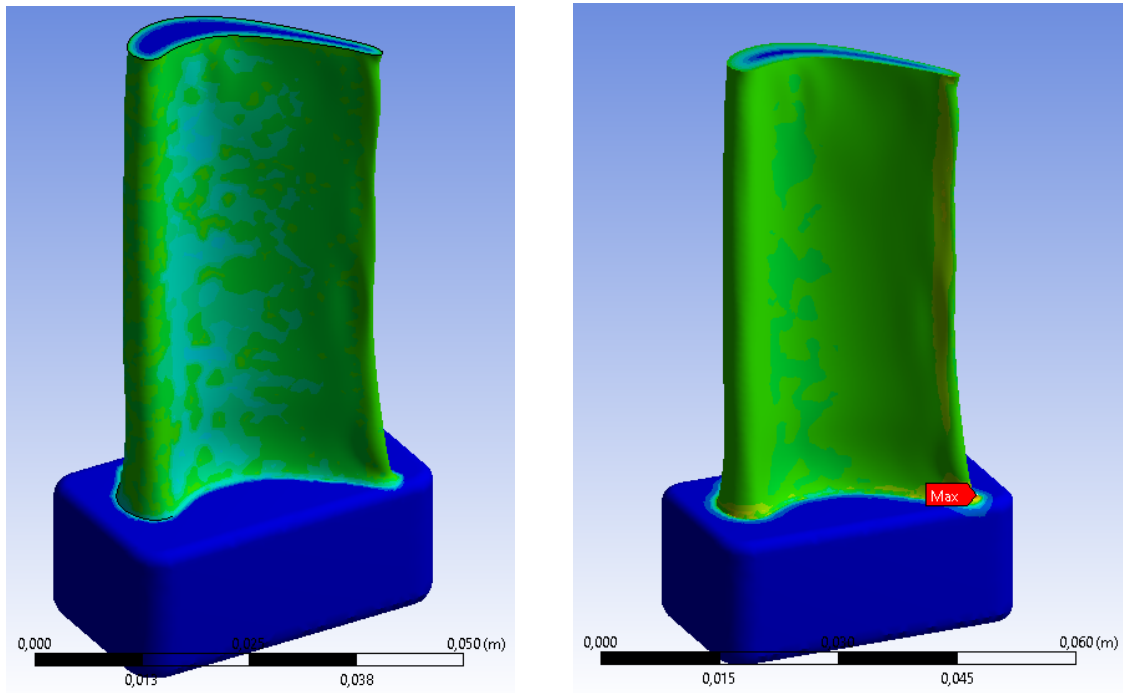
Figure 5.22: Blade front heat flux distribution at 0.1 s and at the end of the analysis
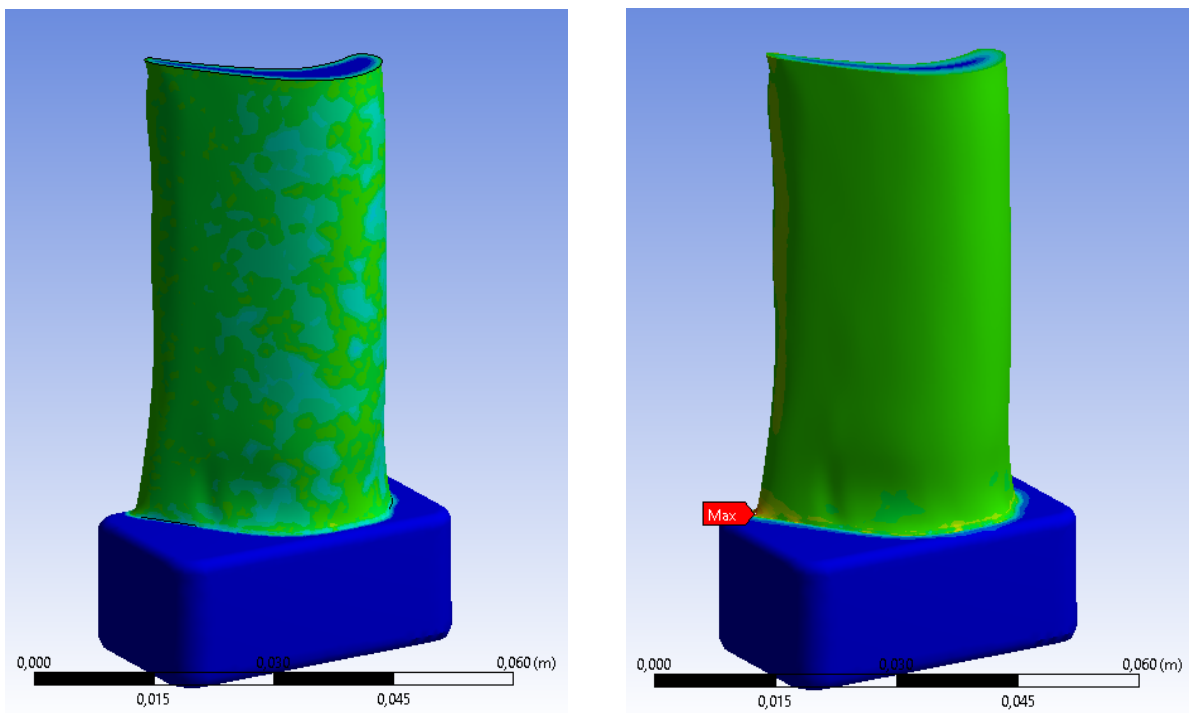
Figure 5.23: Blade rear heat flux distribution at 0.1 s and at the end of the analysis

69
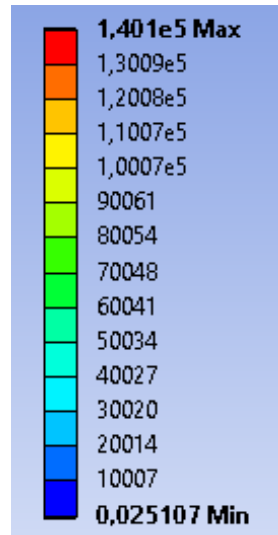
Figure 5.24: Total heat flux values (W/m^2) and respective colours

As shown, the maximum value of heat flux is in the **attachment to the base** of the **trailing edge**.

Time (s)	Total Heat Flux (W/m^2)	Time (s)	Total Heat Flux (W/m^2)
0.03	82531	0.48	$1.17 \cdot 10^5$
0.06	87059	0.55	$1.21 \cdot 10^5$
0.08	88350	0.61	$1.24 \cdot 10^5$
0.15	91839	0.68	$1.27 \cdot 10^5$
0.21	98623	0.75	$1.3 \cdot 10^5$
0.28	$1.04 \cdot 10^5$	0.81	$1.33 \cdot 10^5$
0.35	$1.09 \cdot 10^5$	0.88	$1.36 \cdot 10^5$
0.41	$1.13 \cdot 10^5$	0.95	$1.38 \cdot 10^5$
	Continues...	1	$1.401 \cdot 10^5$

Table 5.8: Maximum heat flux values over time

The graph in Figure 5.25 represents graphically the values of Table 5.8, in a heat flux over time graph.
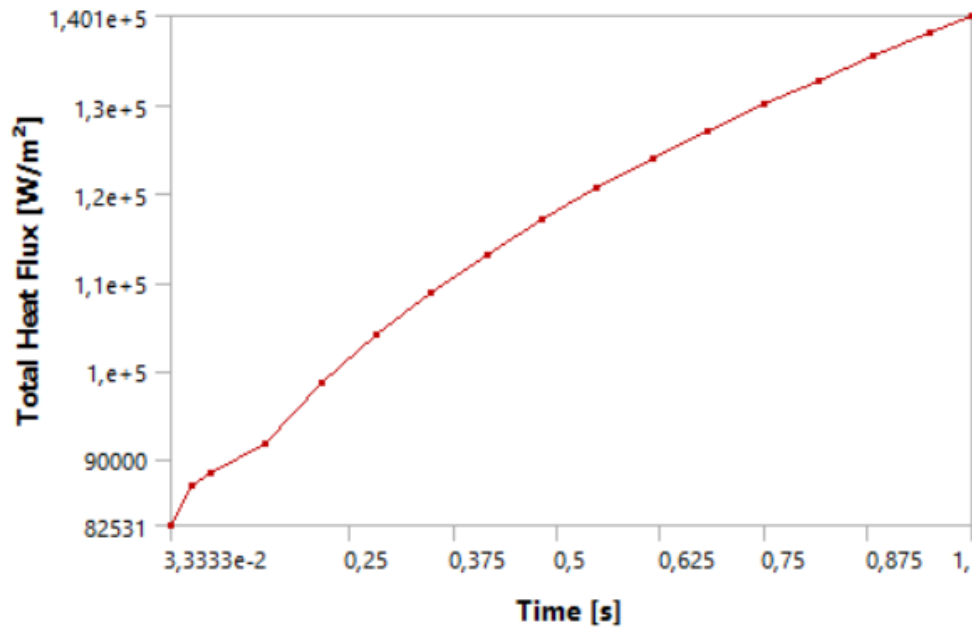
Figure 5.25: Total heat flux over time graph

72

Conclusions and Future Developments

The results given by the analyses proved to be consonant with the values that can be found in literature. The stress-strain curve, which is linear, is composed of values that resemble experimental curves. Moreover, the results of both analyses depict a realistic representation of the behaviour of the blade in the high mechanical and thermal stress environment in which it operates.

A lot of research and progress is being made by designers in material science for these particular applications. Thanks to their low density (confronted with that of superalloys) and high mechanical and thermal strengths, *composite materials* for uses in combustion chambers and jet turbines have emerged over recent years. These materials are composed of a Al_2O_3 or SiC matrix, coupled with fibers of the same material in order to avoid different coefficients of thermal expansion. They are able to operate at 100-200 °K more than regular superalloys. This allows to have a more thermically efficient propulsion unit, as less air would be spilled from the compressor in order to cool the hotter parts of the engine; it could allow to increase the bypass flow, increasing the propulsive efficiency and lower the NO_x emissions as well. Research currently focuses on optimization of manifacturing processes of these materials: the most common process is *reactive melt infiltration*, which allows to have a product with low residual porosity but limits the use in high-temperature environments due to the low melting point of the product.

Another very interesting and quite new manufacturing process is *additive layer manufacturing* (or 3D printing) which allows to create a three dimensional object with layers of material controlled by a computer.

The production of high-temperature resistant materials widely used in aircraft combustion chamber and turbines, like the iron-nickel base superalloy Inconel 718 and Titanium 64, is being tested with this method. Mechanical properties are found to be equal or greater of those of thier cast or wrought counterparts. The use of ALM allows the production of complex geometries with a lot more freedom and ease, also reducing significantly the amount of wasted material during production.

But, unfortunately, at the present stage, ALM turbine blades are not able to withstand the extreme mechanical stresses associated with rotating parts, as their creep resistance is not enough. Further research and tests need to be performed in order for this technology, in the future, to be able to be widely implemented in commercial aviation.

Bibliography

[1] Davide Boiani. Relazione Finale di Tirocinio. 2017.

[2] J. V. Kelley D. P. Dandekar, A. G. Martin. High temperature elastic properties of polycrystalline MAR-M200 (a Nickel Base superalloy). *Metallurgical Transactions A*, 12A, 1981.

[3] Saeed Farokhi. *Aircraft Propulsion, Second Edition*. Wiley, 2014.

[4] D. Pratt J. Mattingly, W. Heiser. *Aircraft Engine Design, Second Edition*. AIAA Education Series, 2002.

[5] S. Donachie M. Donachie. *Superalloys: A Technical Guide, Second Edition*. 2002.

[6] A. F. Giamei M. Gell, D. N. Duhl. The development of single crystal superalloy turbine blades. *Superalloys*, 1980.

[7] Pratt & Whitney. Type certificate data sheet E20EA. 2000.

[8] Frank W. Zok. Ceramic-matrix composites enable revolutionary gains in turbine engine efficiency. *American Ceramic Society Bulletin*, 95(5), 2016.

Acknowledgements

First of all, I would like to greatly thank every single one of my professors who, with their dedication and passion, taught me a lot and helped me become the person I am today.

I especially want to thank Prof. Enrico Troiani for his constant availability, great sense of humor and high professionality.

Then, I would like to thank by heart my parents, for their patience and costancy in spurring me to become a better person.

I also would like to thank my wonderful girlfriend, Serena, for always supporting me through difficult times, for being there when I needed it and always having my back. A big thank you to all my dear friends and colleagues that accompanied me throughout this years, with whom I shared great experiences.

A special thanks goes to Prof. Giovanni Carlo Bonsignori who, over the years, with his dedication and love for science, has been a great inspiration and example.

This thesis is dedicated to my grandfather, Carlo. He would have loved to see me graduate; now, when looking down on me, I am sure that he is happy.